MASTER THESIS

MANIPULATION OF SOFT GRIPPERS FOR PICK-AND-PLACE TASKS

Frank van den Brink

FACULTY OF ENGINEERING TECHNOLOGY
DEPARTMENT OF BIOMECHANICAL ENGINEERING

EXAMINATION COMMITTEE
Prof. Dr. S. Misra
F. Ongaro MSc
Dr. S. Scheggi
Prof. Dr. G. Krijnen

DOCUMENT NUMBER
BW - 511

UNIVERSITY OF TWENTE.

10-03-2016

Manipulation of soft grippers for pick-and-place tasks

Frank van den Brink
University of Twente, The Netherlands

***Abstract*— Micro-sized agents, such as magnetic micro-robots, provide new opportunities in the fields of biological micro-manipulation and minimally invasive surgery (e.g., micro-manipulation of cells and ophthalmic microsurgery). In order for these agents to perform accurate minimally invasive operations, precise control feedback and tracking algorithms are required. In this work we investigate tracking and control of soft grippers. These miniaturized grippers open and close reversibly by heat and can be used to grasp and release micro sized objects at precise locations or deliver drugs to specific locations inside the human body. Furthermore the soft nature of the grippers allows them to handle human tissue without damaging it. This makes them interesting for biopsy applications. The grippers are magnetized so that their position can be controlled remotely by using external magnetic fields. The aim of this study is to precisely track and control the grippers and use them as carriers to autonomously pick-and-place micro-beads and to grasp and release biological tissue while avoiding obstacles in a 2D workspace. Camera image guidance is used to track the gripper position. A Peltier element is used to control the temperature of the workspace and the self-folding property of the grippers. The grippers are controlled using external magnetic fields provided by six orthogonal electromagnets. We achieved to control the grippers with an average velocity of 680 ± 123 μm/s, a set-point error of 108 ± 99 μm and a region of convergence (ROC) of 129 ± 56 μm. Pick-and-place of biological tissue was executed with an average execution time of 130 ±39 s and average drop off error of 626 ± 226 μm. Furthermore for the autonomous pick-and-place experiments 3 micro-beads of different colors were sorted with an average execution time of 437 ± 105 and a precision of 1215 ± 681μm.**

I. Introduction

The field of untethered micro-robotics is widely researched and its development has been evolving fast during the last decade [1]. Micro-sized agents can be used in applications, such as micro-manipulation and minimally invasive surgery. They can be employed to be steered towards hard to reach places in the human body for targeted drug delivery, brachytherapy, manipulation of cells, and removal of deposits in blood vessels [2]. Wireless power supply, imaging in the human body, and actuation at micro-scale represent the main challenges for these micro-robots. Control and visual and ultrasound tracking of micro-particles [3], self-propelled micro-jets [2], [4]–[6] and sperm-driven micro-robots [7], [8] has been achieved. And even realistic clinical cases have been approached [9]. The motion of micro-robots can be induced by magnetic field gradients (micro-particles), rotating magnetic fields (magneto-tactic-bacteria and sperm-driven micro-robots [10]) or conversion of chemical energy to kinetic energy (self-propelled micro-jets). The direction of self-propelled micro-jets is controlled by applying weak magnetic fields to which the micro-jets align.

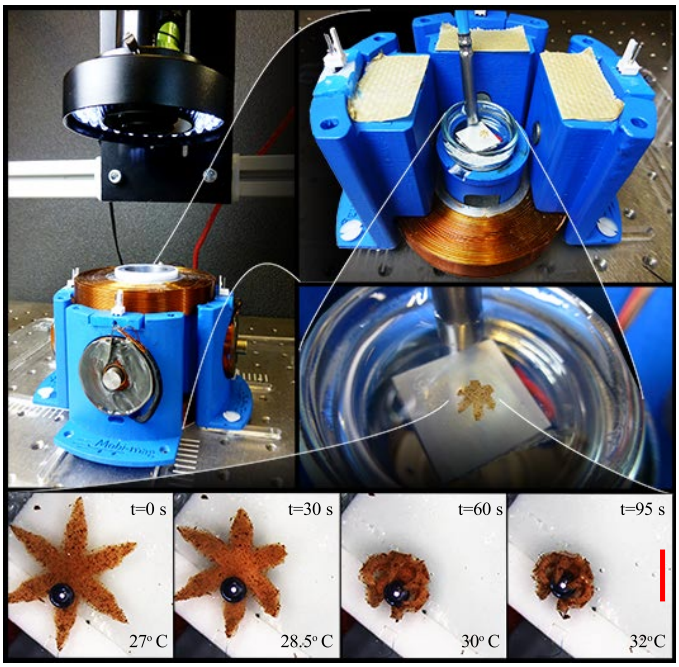

Fig. 1: Top: photographs of the electromagnetic and thermal systems used to control the grippers. The system consists of 6 orthogonal electromagnets to control the gripper position, and a Peltier element to control water temperature inside the petri dish to open and close the grippers. Bottom: Video snapshots of a gripper grasping a microbead. The scale bar is 800 μm.

Since micro-robots can be controlled with high precision they are also interesting for micro-manipulation tasks. Micro-robots can be used as carriers for transportation and assembly at micro-scale. Sanchez *et al* demonstrated micro-manipulation with micro-robots by using catalytic micro-bots for transportation of animal cells to desired targets [11]. Furthermore micro-assembly tasks has been demonstrated with clusters of micro-particles and swarms

of flagellated bacteria [12], [13]. The above micro-robots are limited in options. They are only capable of moving objects by pushing resulting in trivial micro-manipulation tasks. In order to expand the micro-manipulation tasks, research to miniature robots with grabbing functionality is carried out. Grabbing functionality would expand options in targeted drug delivery (as the drug can be released), biopsy (tissue sample can be grabbed), and micro-manipulation (objects can be grabbed and delivered at a target location). Miniature agents with grabbing functionality have been developed and used in *in vivo* experiments [14]–[16], but are relatively large (cm scale) however. Down-scaling is a challenge since these robots need batteries to power actuation. In order to avoid this power supply problem, Gracias *et al* introduced grippers with different self-folding mechanism techniques based on capillary forces, thin film stress mismatch, and swelling [17]–[20]. These grippers consist of different layers which either expand or contract, under the influence of pH-level or heat, making them open or close.

Grippers make it possible to take sample tissue from hard to reach places within the human body *e.g.* the lungs. Ideal sizes for the grippers for this kind of operation would be in the range of 10 μm to 1 mm tip-to-tip since the sizes of cells are in the range of 10 - 100 μm [21]. Gultepe *et al* performed biopsy with manually controlled metal grippers with sizes ranging from 300 μm to 1.5 mm tip-to-tip in a porcine model [21]. These metallic grippers were first cooled to stay open, and then closed irreversibly after being exposed to body temperature for 10 minutes. The grippers were injected into the duodenum of the animal using a catheter that was guided from the mouth to the duodenum. The grippers were able to retrieve sample tissue with a retrieval rate of 95%. The not retrieved grippers can harm the human body since they are not bio-compatible.

Also it is important to not damage retrieved tissue for reliable biopsy results. Therefore for this study grippers of soft material are investigated. The soft grippers are made from hydrogel paired with a rigid non-swelling polymer and are patterned with iron-oxide. Hydrogel is a soft bio-degradable material which changes volume with changing temperature. This swelling properties make hydrogel very suitable for gripping mechanisms.

For this thesis the grippers are employed for pick-and-place and autonomous sorting of different colored polystyrene micro-beads. Also the grippers will be used as carriers for pick-and-place of egg yolk while avoiding obstacle. These experiments demonstrate the soft nature and grabbing and positioning capabilities of the grippers. Furthermore these experiments demonstrate the magnetic system's tracking, positioning and thermal control capabilities.

II. Contributions

During this study the following contributions were made:

- Precise 2D motion control of grippers.
- Precise positioning of micro-beads using grippers.
- Employment of grippers for pick-and-place of biological tissue while avoiding obstacles using path planning.
- Autonomous sorting of different colored micro-beads using grippers.
- Control of grippers using a haptic device.

These contributions resulted in the following scientific publications:

F. Ongaro, S Scheggi, C. Yoon, F. van den Brink, D. H. Gracias and S. Misra, "Autonomous Planning and Control of Soft Untethered Grippers for Potential Applications in Dynamically-Cluttered Environments", in *Applied Physics Letters (APL)*, *Under review.*

F. Ongaro, C. Yoon, F. van den Brink, M. Abayazid, S. H. Oh, D. H. Gracias and S. Misra, "Control of Untethered Soft grippers for Pick-and-Place Tasks", in *IEEE RAS/EMBS International Conference on Biomedical Robotics and Biomechatronics (BioRob)*, Singapore, June 2016, *Under review.*

C. Pacchierotti, F. Ongaro, F. van den Brink, C. Yoon, D. Prattichizzo, D. H. Gracias and S. Misra, "Steering and control of soft magnetic grippers with haptic feedback", in *The International Journal of Robotics Research (IJJR)*, *Under review.*

C. Yoon, F. van den Brink, R. Xiao, T. D. Nguyen, S. Misra, and D. H. Gracias, "Untethered thermo-magnetically responsive hydrogel grippers", in *Proceedings of the Materials Research Society (MRS) Fall Meeting and Exhibit*, Boston, USA, November-December 2015.

III. Thesis outline

The remainder of this thesis is organized as followed: Sec. IV provides an overview of the materials and experimental methods used for this study and Sec. V shows the achieved experimental results. Then Sec. VI provides a discussion of the experimental results and finally Sec. VII concludes this work and gives directions for future work.

IV. Materials and methods

In this section we will introduce the experimental set-up, and the grippers used in this work. Then we will present the tracking algorithm, the control law and the path planning algorithm used to detect and move the agents, respectively. Finally we will present the experimental plan we made to demonstrate the capabilities of the grippers and the magnetic system.

A. Experimental set-up

The experimental set-up consists of the Mobimag system and a haptic interface. The Mobimag system is capable of actuating electromagnets and a Peltier element to control the magnetic field gradients and the temperature of the workspace. This makes it possible to control both motion and configuration (e.g. open or closed) of the grippers. The haptic interface can be connected to the Mobimag system in order to provide position- as well as temperature set-points to the Mobimag system.

1) Mobimag system: The Mobimag magnetic set-up (Fig. 1) consists of 6 orthogonal electromagnets and is capable of providing magnetic fields and magnetic field gradients of 15 mT and 60 mT/m, respectively. Each electromagnet is powered by an Elmo Whistle 1/60 servo controller (Elmo Motion Control, Petach-Tikva, Israel). The current provided by the Elmo servo controller is calculated using a PID-controller and reaches a maximum of 1 A. The workspace of the grippers is a petri dish filled with water surrounded by the electromagnets. To be able to heat and cool the water the petri dish is connected to a Peltier element which is powered and controlled on low level by an Arduino Uno (Arduino, Ivrea, Italy) microcontroller. The microcontroller is provided with a temperature setpoint which is determined by the desired configuration of the gripper. The temperature control is able to achieve a steady-state error of about 1 °C and can heat the water at averagely 10 °C/min. A temperature probe is used to measure the water temperature to provide feedback. Furthermore a Blackfly 1.4 MP Color GigE PoE (Point Grey Research Inc., Richmond, Canada) camera is mounted on a Mitutoyo FS70 microscope unit (Mitutoyo, Kawasaki, Japan) using a Mitutoyo M Plan Apo 2 / 0.055 Objective is mounted above the petri dish for visual tracking of the grippers. The camera provides a field of view of 1.2 × 1.2 cm.

2) Haptic system: The haptic feedback system is a 6-DoF (Degrees of Freedom) Omega haptic interface (Force Dimension, Switzerland), shown in Fig. 2. It is composed of a delta-based parallel kinematics structure that provides good closed loop stiffness and high accuracy. The rotating wrist joint allows the user to also change the orientation of the pen-shaped end-effector. Moreover, the

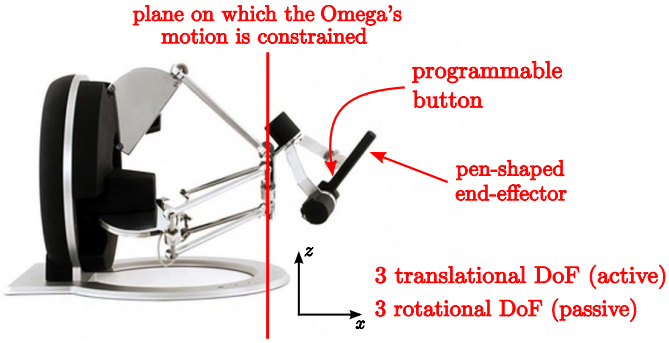

Fig. 2: Omega 6 haptic interface: The haptic interface provides the human operator with haptic feedback from the remote environment and, at the same time, provides the control system with the grippers's reference position. Moreover, the pen-shaped end-effector is used to control the target temperature of the environment. Since the grippers are controlled in 2D space, we constrained the translational motion of the Omega to its x-y plane.

interface is constructed in such a way that translations and rotations are decoupled from each other. Translational degrees of freedom are active, while rotational degrees of freedom are passive. This haptic interface is also equipped with active gravity compensation to improve the teleoperation transparency and reduce the operator's fatigue. In this work we use the Omega 6 interface as an impedance haptic device. We measure the position of the end-effector, controlled by the human operator, to set the reference target position of the gripper. The scaling factor between master and slave systems is 0.2 in all directions, i.e., moving the end-effector of the Omega interface of 10 cm moves the gripper's reference position of 2 cm. At the same time, through the same end-effector, we provide the operator with force feedback from the remote environment. The force to be provided is evaluated according to the feedback condition considered, as detailed in Sec. IV-F.6, and it is a combination of kinesthetic, frictional, and vibrotactile stimuli. The haptic control loop runs at 2 kHz.

Since we control the grippers in 2D space, the translational motion of the Omega is constrained on a x-y plane (see Fig. 2). Force $f_z(t)$, provided by the Omega interface along the z axis, is defined as

$$f_z(t) = -k_{b,k}(p_{r,z}(t) - p_{z,plane}),$$

where $k_{b,k} = 1000$ N/m, $p_{r,z}(t)$ is the current position of the end-effector of the Omega in the z direction, and $p_{z,plane}$ is the location of the x-y plane along z. The Omega's pen-shaped end-effector is also equipped with a programmable button, which is used during the experiments to activate/deactivate the temperature control on the Petri dish (see Sec. IV-D). When the temperature

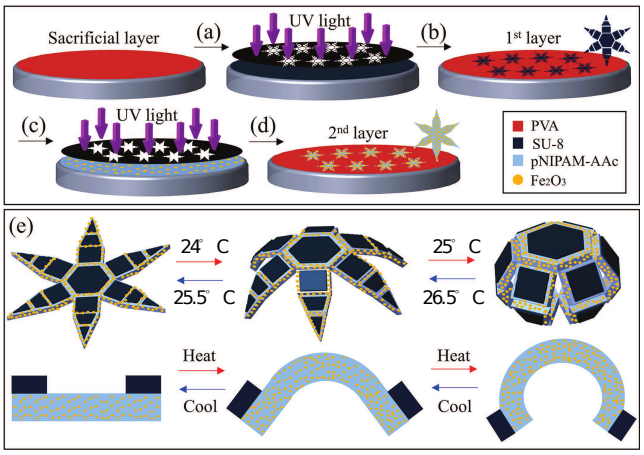

Fig. 3: A schematic for the fabrication process of the soft grippers: (a) SU-8 is spin-coated on a polyvinyl alcohol (PVA) sacrificial layer. (b) The SU-8 film is photopatterned and exposed to ultraviolet (UV) light. (c) A 95% poly-N-isopropylacrylamide (pNIPAM-AAc) and 5% biocompatible iron oxide layer is allocated on the SU-8 layer. (d) The coated surface is photopatterned and exposed to UV light to obtain dry bilayer grippers. (e) Schematic images of the untethered grippers in open and closed (grasping) configurations. Also shown is a side-view of a single hinge.

control is active, the pen-shaped end-effector enables the human operator to control the target temperature of the environment. The end-effector can rotate, and its orientation is used to set the target temperature driving the Peltier element to

$$t_{pe} = \left(\frac{\theta_r}{60} + 36\right), \tag{1}$$

where $\theta_r \in [0°, 320°]$ is the rotation of the pen-shaped end-effector (see Fig. 2). More details on how the temperature control works can be found in Sec. IV-D. As mentioned, controlling the temperature of the environment enable us to open and close the grippers.

B. Grippers

This section will describe the properties and fabrication process of the different gripper samples as well as the the motion modeling of the grippers.

1) Fabrication: The grippers are fabricated from SU-8/continuous pNIPAM-AAc bilayer patterns which allows the grippers to open and close reversibly by heating and cooling. The grippers are patterned with 5 % w/w iron-oxide to give them magnetic properties and are 4 mm tip-to-tip. In order to fabricate discrete SU-8/continuous pNIPAM-AAc bilayer gripper patterns, initially, 90 % hydrolyzed polyvinyl alcohol (PVA, MW 9-10 kDa, Sigma-Aldrich) sacrificial layer was spin coated onto a Si wafer (WRS) at 2000 rpm and then baked at 115° C for 5 min. Next, SU-8 2015 negative photo resist (MicroChem) was spin coated on the PVA at 2000 rpm to achieve an approximately 21 μm thickness. Pre-baking process was done at 70° C for 1 minute, 115° C for 3 minutes, and 70° C for 1 minute. After this, the SU-8 film was photo patterned by using a discrete gripper shaped dark field mask and exposed to 180 mJ/cm^2 UV light (365 nm) to initiate crosslinking. Subsequently, post-baking was executed at 70° C for 1 minute, 115° C for 3 minutes, and 70° C for 1 minute. Uncrosslinked portions of the SU-8 were removed using a commercial SU-8 developer (MicroChem) for 1 minute and then washed with acetone (Fisher Scientific) for 1 second and isopropyl alcohol (IPA, Fisher Scientific) for 10 seconds before being dried with compressed air. In order to fabricate the ferromagnetic second layer of poly-N-isopropylacrylamide (pNIPAM-AAc), 5 % w/w biocompatible iron (III) oxide (Fe2O3, Sigma-Aldrich) nanoparticles were incorporated into the pNIPAM-AAc solution. The pNIPAM-AAc solution was prepared by mixing 3 g N-isopropylacrylamide monomer (NIPAM, Scientific Polymer Products Inc.), 0.4 g poly-N-isopropylacrylamide (pNIPAM, 300 k MW, Scientific Polymer Products Inc.), 0.18 g N-Methylenebis-Acrylamide (BIS, Sigma-Aldrich), and 0.31 ml acrylic acid (AAc, Sigma-Aldrich) in 7.5 ml n-butanol (Sigma-Aldrich) followed by stirring it for 10 hours at room temperature. In order to achieve uniform thickness (34 μm) of the pNIPAM-AAc layer, 800 μl pNIPAM-AAc including Fe2O3 was allocated on the discrete SU-8 patterns/Si wafer for 1 minute. The obtained pNIPAM-AAc solution including Fe2O3 was patterned on the previously photopatterned SU-8 segments using a second dark field mask and aligned in non-contact mode using spacers. In order to initiate crosslinking the deposited and aligned pNIPAM-AAc solution was then exposed to 40 mJ/cm^2 UV light. Then uncrosslinked parts were removed by washing with acetone and IPA before drying using compressed air. Finally, the wafer was immersed in DI water overnight to completely dissolve the PVA sacrificial layer making it possible to collect free-standing SU-8/pNIPAM-AAc grippers. Fig. 3 shows a schematic view of the above mentioned fabrication process.

2) Motion modelling: The motion of a gripper is governed by

$$\mathbf{F}(\mathbf{P}) - \mathbf{F}_d(\dot{\mathbf{P}}) - F_b\hat{\mathbf{n}} = M\ddot{\mathbf{P}} \tag{2}$$

$$\tau(\mathbf{P}) - \tau_d(\dot{\omega}) = I\ddot{\omega} \tag{3}$$

where $\mathbf{F}(\mathbf{P}) \in \mathbb{R}^{3\times1}, \mathbf{F}_d(\dot{\mathbf{P}}) \in \mathbb{R}^{3\times1}$ and $F_b \in \mathbb{R}$ are the magnetic force, linear drag force and buoyancy force at position $\mathbf{P} \in \mathbb{R}^{3\times1}$. Furthermore M is the mass of the gripper and $\hat{\mathbf{n}} \in \mathbb{R}^{3\times1}$ is the unit vector. In Equation (3)

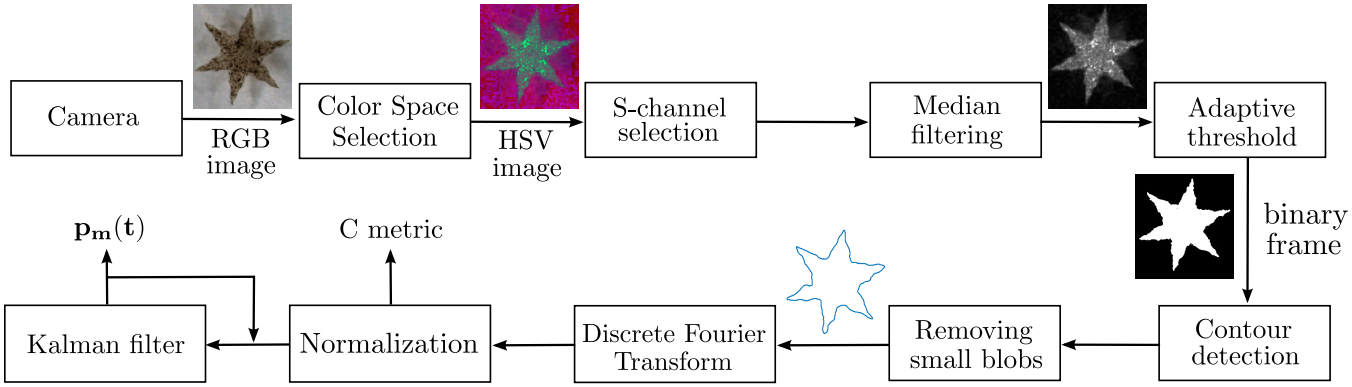

Fig. 4: Tracking algorithm. Each frame registered by the high-resolution camera is first converted to HSV colorspace, then its saturation channel (S) is filtered using a median filter, and a binary frame is obtained using an adaptive threshold. The binary frame is then used to find the contours of the image, and Fourier descriptors are computed to detect the centroid of the gripper and measure how much the gripper is closed. Finally, a Kalman filter is used to deal with uncertainties in the tracking.

$\tau(\mathbf{P})$, $\tau_d(\dot{\omega})$ and I are the applied torque, rotational drag force and rotational inertia of the gripper. The magnetic force and torque acting on the gripper depend on the strength of the magnetic field according to:

$$\mathbf{F}(\mathbf{P}) = \nabla(\mathbf{m}(\mathbf{P}) \cdot \mathbf{B}(\mathbf{P})) \tag{4}$$

$$\tau(\mathbf{P}) = \mathbf{m}(\mathbf{P}) \times \mathbf{B}(\mathbf{P}) \tag{5}$$

where $\mathbf{m}(\mathbf{P})$ is the magnetic dipole moment of the gripper and ∇ is the gradient operator. In Equation (2) and (3) the linear and rotational drag forces are given by

$$\mathbf{F}_d(\dot{\mathbf{P}}) = \alpha_{dl}\dot{\mathbf{P}} \text{ and } \tau_d(\dot{\omega}) = \alpha_{dr}\dot{\omega} \tag{6}$$

where α_{dl} and α_{dr} are the linear and rotational drag force coefficients respectively. The magnetic field $\mathbf{B}(\mathbf{P})$ in Equation (4) and (5) is related to the current through the electromagnets by an actuation matrix. Control of the magnetic field will be explained into more detail in Sec. IV-D.

C. Tracking

This section describes the steps used to track the grippers and recognize their configuration (open or closed). The grippers are tracked and recognized using Fourier descriptors. Fourier descriptors are a technique which uses the description of an image in the frequency domain. In order for the Fourier descriptors to give good results it's important that a clear contour of the grippers is computed. The Fourier descriptors are used to find the center, perimeter and area of the grippers and recognize their configuration. Fig. 4 provides an schematic overview of the steps taken to track the grippers. The remainder of this section explains each step into more detail.

1) Color space selection: Due to lightning changes in the background and glare from the SU8-layer of the grippers it was hard to track the grippers robustly in RGB-colorspace. The RGB color model is in fact an additive model in which red, green, and blue lights are added together. For this colorspace it is not trivial to separate the intensity information from the color information, making the model quite sensitive to changes in the light condition [22]. To address this problem, we looked into HSV- and YUV-colorspace which both separate *luma* (intensity) information from *chroma* (color) information. In order to decide which color space would be best for robust tracking we converted an RGB-image to HSV- and YUV-colorspace. From these images we computed the histograms (Fig. 5). For this work different gripper samples were used with all different appearances due to different fabrication methods and different iron-oxide percentages. Therefore thresholding was done on the surroundings of the grippers. In order to find the dominant color value of the background in all 9 color channels an image with a high amount of background was used for the histograms. From Fig. 5 it can be seen that opposed to the RGB- an YUV color space there is a very clear distinction between one channel (S-channel) and the other two channels in the HSV-colorspace. Therefore we use the HSV color space to track the grippers. The HSV color model, introduced by [23], approximates the perceptual properties of "hue," "saturation," and "value:"

- Hue associates the color with a position in the color spectrum (red, green, and yellow are hue names).
- Saturation describes the "vividness" of a color, pure spectral colors being "fully saturated colors" and grays being "desaturated colors".
- Value corresponds to the "lightness" of a color.

From the original RGB image, we can calculate the S-channel as

$$\begin{cases} S = 1 - \dfrac{\min(R,G,B)}{\max(R,G,B)} & \text{if } \max(R,G,B) > 0 \\ S = 0 & \text{if } \max(R,G,B) = 0. \end{cases} \tag{7}$$

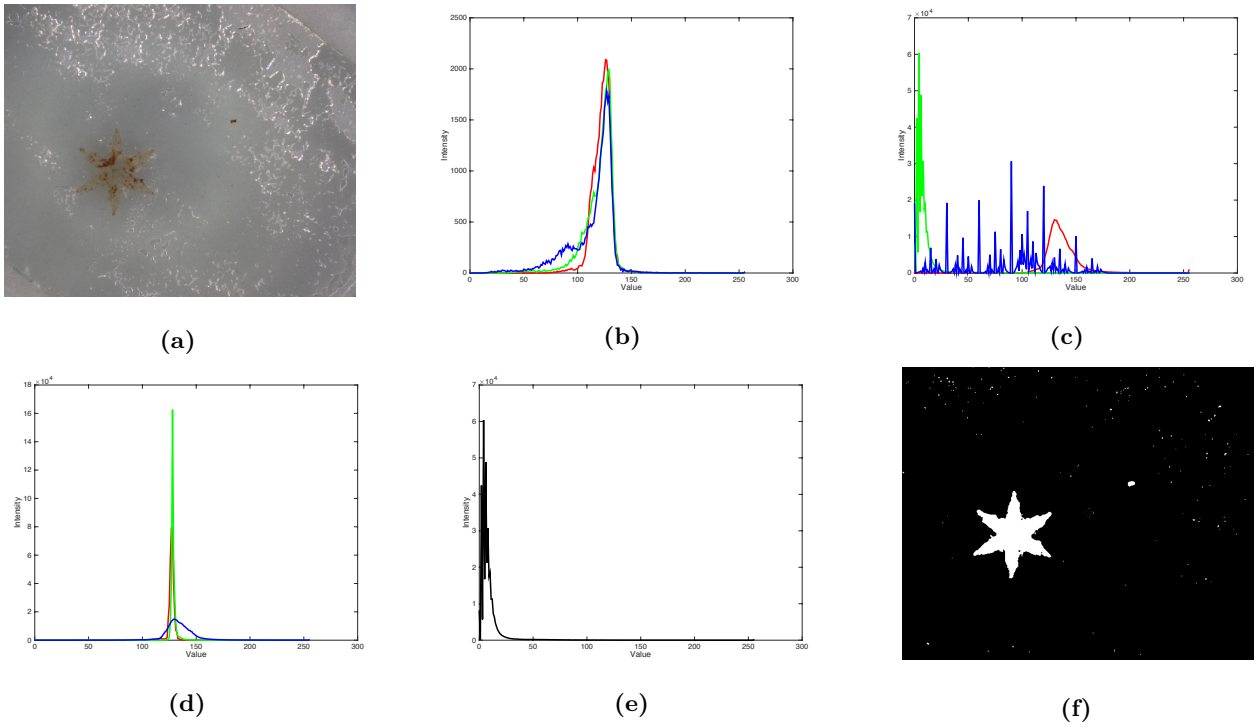

Fig. 5: Comparison of histograms of a gripper in the workspace in different colorspaces. (a) The original RGB-frame captured from the high resolution camera. (b) RGB-histogram. (c) HSV-histogram. (d) YUV-histogram. (e) Histogram of the S-channel. (f) Binary image obtained from threshold=30. In subfigures (b)-(d) the red, green and blue lines indicates the intensities of the RGB, HSV and YUV channels. To point out the use of the S-channel this one is pointed out in (e). (f) shows the result of thresholding the image.

An experimental comparison of the most popular color models can be found in [24]. For the example image, S-intensity <50 is very strongly present. Since most of the image is occupied by surroundings of the gripper we can conclude that S-values < 50 do not represent the gripper. Thresholding the image around this value removes the background and makes it possible to robustly compute the contour as can be seen in Fig. 6. In order to get this result for each frame we used an adaptive threshold.

2) Median filtering: After converting the image from RGB- to HSV-color space and extracting the S-channel from the HSV-image a median filter is applied to reduce noise. A median filter replaces each pixel value with the median of a $n \times n$ neighborhood where $n = 20$ represents the kernel size of the filter. Fig. 6c shows the median filtered S-channel of the HSV-image (Fig. 6b).

3) Adaptive thresholding: Now that the S-channel of the HSV-image is extracted and the noise is reduced, the image is binarized using adaptive thresholding. The filtered S-channel $F_s(x, y)$ is converted to a binary frame $F_b(x, y)$ by

$$F_b(x,y)(x,y) = \begin{cases} 255 & \text{if } F_s(x,y) > T(x,y) \\ 0 & \text{otherwise} \end{cases} \quad (8)$$

where 0 is the value for black and 255 is the value for white color in the image. Furthermore $T(x, y)$ is the threshold matrix defined as the the weighted average of neighborhood values around the considered pixel. The average is weighted using a Gaussian window.

4) Contour detection: From the binary image, we compute the contours of all the visible blobs using the contour detection algorithm implemented in the OpenCV function `findContours()`. The algorithm is based on the technique presented by [25] and then further developed by [26] and [27]. Each blob is described by a sequence of points connected to each other by segments. This sequence is found using the method proposed by [28], in which the detected objects are represented as trees. In each tree, the root is a sequence describing the outer contour, and the children are sequences describing inner contours of successive levels. The algorithm of [28] is based on two main identifiers, referred to as NBD and LNBD. The NBID identifier is the sequential number of a newly-found border, while the LNBD identifier is the sequential number of the border most recently encountered during the searching process. Once a new border is found, it is assigned with the uniquely identifiable number NBD. During the scan, also the sequential number LNBD of the

border encountered most recently is kept. This memorized border should be either the parent border of the newly-found border or a border which shares the common parent with the newly-found border. The searching process is performed in a scanning manner. The binary image is scanned with a given raster starting with the NBD identifier set to 1. LNBD is then reset to 1 every time a new row of the image is analyzed. Finally, to approximate the segmented contour to the real shape of the blob, we use the L1 metric chain approximation algorithm presented by [29]. Once the contours are computed, blobs whose contour is smaller than a gripper are removed, leaving out only our target gripper. Fig. 6e shows the image after the above mentioned contour detection process.

5) Fourier Descriptors: For this work Fourier descriptors are used for:

- Finding the center of the gripper.
- Recognizing the configuration of the gripper.

In order to calculate the Fourier descriptors of a given contour its x- and y-coordinates first are re-sampled to 32 values and then mapped to the imaginary plane. In the imaginary plane the $x-$coordinates represent the real values and the $y-$coordinates the imaginary values:

$$z(s) = x(s) + iy(s) \tag{9}$$

where x and y are the contour coordinates and i is the imaginary number. Furthermore s is the running arc length (sampled to 32 values). After mapping the coordinates to the imaginary plain a discrete Fourier transform is applied on the coordinates:

$$Z_k = \frac{1}{N}\sum_{n=0}^{N-1} z_n \exp\left(\tfrac{-i2\pi nk}{N}\right) \tag{10}$$

where z_n are the re-sampled boundary points and N is the number of points. The discrete Fourier transform computes 32 imaginary values : $Z_{-15} : Z_{16}$. The center of gravity of the contour can now be found by using Z_0:

$$\begin{aligned} x_c &= Re(Z_0) \\ y_c &= Im(Z_0) \end{aligned} \tag{11}$$

where x_c and y_c are the x- and y-coordinate of the center of gravity of the contour respectively and Re and Im denote the real and imaginary values. The Fourier descriptors are used to recognize if the grippers are open or closed. An useful feature of the Fourier descriptors is that they can be normalized to make them translational-, rotational-, and scale invariant. In order to compute these normalized Fourier descriptors we carried out the following steps: [30]:

- *Position:* Z_0 gives the position of the center of gravity of the contour. Setting $Z_0 := 0$ makes the Fourier descriptors translational invariant. Z_0 is used for the tracking of the grippers.
- *Size (scale):* $Z_k := \frac{Z_k}{|Z_1|}$
- *Orientation and starting point:*

1) Z_1 is the largest Fourier descriptor. Z_L is the second largest.
2) Set $\theta_1 = \arg Z_1$ and $\theta_2 = \arg Z_L$
3) $\beta = \frac{\theta_1 - \theta_2 + 2\pi m}{L-1}$ with: $m = 0, ..., |L-1| - 1$
4) $\alpha = -\theta_1 - \beta$

Now set $Z_k = Z_k \exp[j((k-L)\theta_1 + (1-k)\theta_2)/(L-1)]$

Gripper configuration can now be determined by symmetry and the ratio between the perimeter and area of a computed contour ($R_{PA} = \frac{perimeter}{area}$). These metrics are very suited because they both are scale invariant. Symmetry of a detected contour can be determined using the Fourier descriptors according to the following theorem [30]:

If a contour is M-fold symmetric: $z(s) = z(s)\exp(\frac{2\pi ni}{M})$ where n is an integer, then only the harmonics $1 \pm mM$ where m is an integer, are non-zero.

Since a gripper is approximately 6-fold symmetric this means that only the harmonics 1, -5, 7, -11, 13.. should be nonzero. From Fig. 7 it can be seen that Z_1, Z_{-5} and Z_7 indeed are the largest Fourier descriptors for grippers in open configuration. Since $Z_1 = 1$ for each symmetry and displaying it would make the vertical scale of the diagram too large this descriptor is not displayed.

In order to determine the configuration of a gripper we use both the R_{PA} and a 6-fold symmetry metric (6_{FS}). A gripper is considered to have an open configuration if the following condition is met:

$$6_{FS} > \alpha Z_{k,mean} \quad \&\& \quad R_{PA,mean} > t_{PA}, \tag{12}$$

where $Z_{k,mean}$ is the average of the Fourier descriptors and α and t_{PA} are constants which are determined experimentally. The 6-fold symmetry metric (6_{FS}) is computed as

$$6_{FS} = \frac{1}{m}\sum_{\substack{t= \\ t_c-m+1}}^{t_c} |Z_{-5,t}| + |Z_{7,t}|, \tag{13}$$

where t is the frame number, t_c is the current frame number and m is the number of frames over which the metric is taken. Furthermore in Equation (12) $R_{PA,mean}$ is the moving average of R_{PA} and $Z_{k,mean}$ is computed as:

$$Z_{mean} = \left(\frac{1}{30}\sum_{k=-15}^{16} Z_k\right) - 1 \tag{14}$$

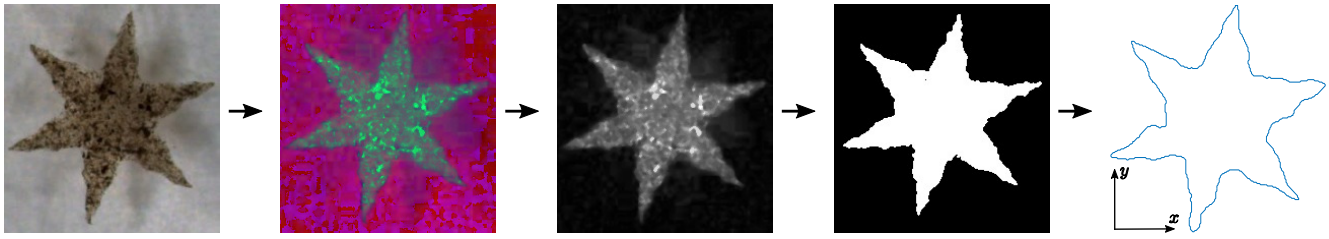

(a) **(b)** **(c)** **(d)** **(e)**

Fig. 6: Tracking algorithm: (a) The RGB image of the gripper, captured by the high-resolution camera, is first converted in (b) HSV color space. Then, (c) its saturation (S) channel is extracted, and it is converted to (d) a binary image using an adaptive threshold approach. Finally, (e) the contour is calculated using the contour detection algorithm presented by [28].

where Z_k are the normalized Fourier descriptors. $|Z_1| = 1$ and $|Z_0| = 0$ are excluded from Z_{mean}. The perimeter P and area A to determine R_{PA} are estimated with the Fourier descriptors by:

$$A = \pi \sum_{k=-15}^{16} k|Z_k|^2 \tag{15}$$

$$P^2 = 4\pi^2 \sum_{k=-15}^{16} k^2|Z_k|^2. \tag{16}$$

6) Kalman Filter: After the center of gravity of the gripper is calculated a Kalman filter is implemented to deal with uncertainties in the tracking. With the Kalman filter both an estimation of the position of the gripper and and an estimation of the next position of the gripper are computed. The estimation of the position of the gripper is used as the grippers position for the tracker. The estimation of the next position is used to position the region of interest (ROI) in the next frame.

The Kalman filter needs a dynamic model of the gripper. For the implemented Kalman filter the motion of the gripper is modeled as

$$x_k = Fx_{k-1} + w_k, \tag{17}$$

where $x_k \in \mathbb{R}^{4\times1}$ is the state variable and $F \in \mathbb{R}^{4\times4}$ is the transfer matrix. x_k and F are given by

$$x_k = \begin{pmatrix} x \\ y \\ v_x \\ v_y \end{pmatrix}_k, F = \begin{pmatrix} 1 & 0 & dt & 0 \\ 0 & 1 & 0 & dt \\ 0 & 0 & 1 & 0 \\ 0 & 0 & 0 & 1 \end{pmatrix} \tag{18}$$

where x and y are the x- and y-position of the gripper, v_x and v_y are the velocities of the gripper in the x- and y-direction and dt is the time difference between measurements respectively. Furthermore in Equation (17) w_k is the process noise which is a random variable with a Gaussian distribution $N(0, Q)$ where $Q \in \mathbb{R}^{4\times4}$ is a co-variance matrix given by $Q = E[\mathbf{w_k}\mathbf{w_k^T}]$. Not all states in x_k are measured and also measurement noise is considered. The vector of measurements z_k is given by:

$$z_k = Hx_k + v_k, \tag{19}$$

where v_k is the measurement error which also assumed to have Gaussian distributions $N(0, R)$ for co-variance matrix $R \in \mathbb{R}^{2\times2}$ given by $R = E[\mathbf{v_k}\mathbf{v_k^T}]$. Since for the grippers only the position is measured z_k and H look like

$$z_k = \begin{pmatrix} z_x \\ z_y \end{pmatrix}, H = \begin{pmatrix} 1 & 0 & 0 & 0 \\ 0 & 1 & 0 & 0 \end{pmatrix} \tag{20}$$

The tracking system runs at 30 Hz. Sec. IV-C.8 describes how the accuracy of the tracking system is evaluated.

7) Micro-bead tracking: The grippers will also be used to autonomously sort different colored micro-beads. Therefore the system has to be capable of tracking micro-beads and recognizing their color. Tracking of the micro-bead is very similar to tracking of the grippers. This section will explain the differences. Fig. 8 shows a schematic overview of the steps taken for micro-bead tracking. The remainder of this section will explain the steps which need more explanation into more detail.

For micro-bead tracking besides the S-channel also the H-channel of the HSV image is used. The S-channel is still used to create a binary image with an adaptive threshold as explained for the gripper tracking. The difference in creating the binary image is that for micro-bead tracking not only small blobs but also large blobs are removed from the binary image. The resulting binary image contains only the micro-beads and is used to mask the H-channel. The H-channel of the image is used to analyze the color of the micro-beads. We selected the H-channel to analyze micro-bead color because in this channel we noticed the largest spread in image intensity which makes it the most suited channel to robustly identify the three colors. We only use pink, blue and green micro-beads and assign

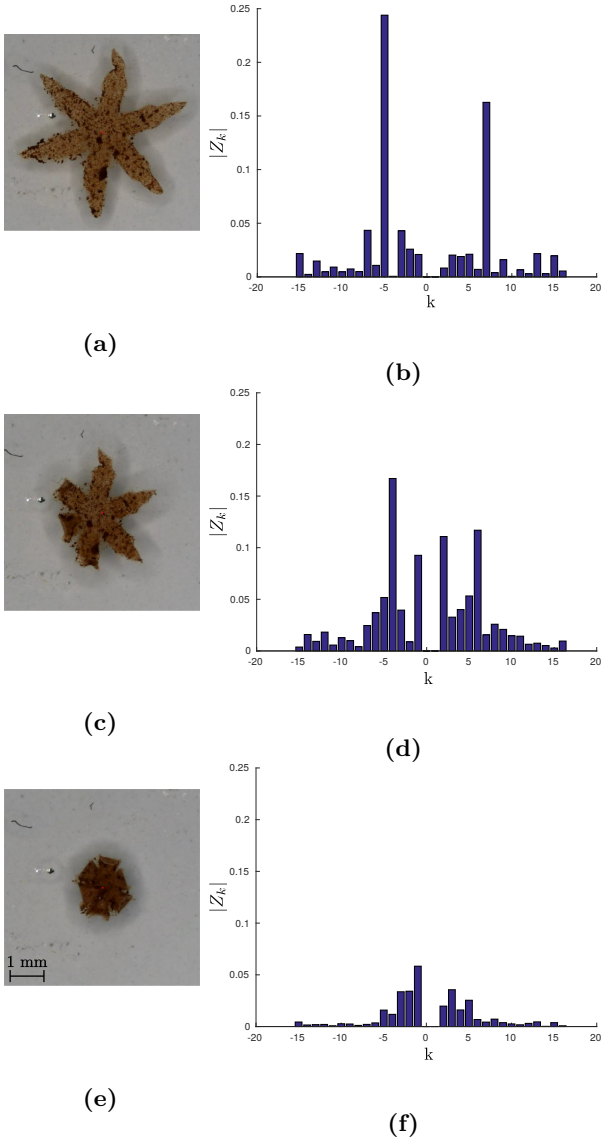

Fig. 7: Three images of the same gripper and their corresponding normalized Fourier descriptors. As the gripper closes, the difference between descriptors $Z_7, Z_{-5}, Z_{13}, Z_{-11}$ and the others descreases. We did not include Z_1 in the graph, since $|Z_1| = 1$, and plotting it would have made the vertical $|Z_k|$ scale too large.

color using thresholds on the intensity in the H-channel:

$$color = \begin{cases} pink & \text{if } H_{val} > T_{pink}, \\ green & \text{if } H_{val} < T_{green}, \\ blue & \text{otherwise,} \end{cases} \tag{21}$$

where H_{val} is approximation of the average intensity of the H-channel inside a blob. Furthermore T_{pink} and T_{green} are threshold values determined by inspecting the H-values of pink and green beads. H_{val} is calculated by:

$$H_{val} = \frac{1}{N} \sum_{\substack{x= \\ c-\frac{\sqrt{2}}{2}R}}^{\substack{c+\frac{\sqrt{2}}{2}R \\ }} \sum_{\substack{y= \\ c-\frac{\sqrt{2}}{2}R}}^{\substack{c+\frac{\sqrt{2}}{2}R \\ }} h(x,y) \tag{22}$$

where N is the total number of summed pixels, R and c are the radius and center of the detected contour and $h(x,y)$ is the H-channel of the frame.

8) Tracker evaluation: In order to evaluate the performance of our gripper tracking system, we registered four videos of four different grippers moving in the workspace, for a total of 281 seconds. We converted the videos to JPEG images at 5 fps, for a total of 1405 images. The centroid of the gripper as tracked by the tracking algorithm and the reference point were not shown. Fifteen participants took part in the experiment, including ten males and five females. None of the participants reported any deficiencies in their visual abilities. The task consisted in looking at the images extracted from the videos and clicking at the centroid of the gripper. The difference between the centroid as estimated by the subjects and the centroid as estimated by our tracking algorithm provides a measure of performance of our tracking algorithm. Each experiment lasted for approximately 30 minutes. The algorithm showed an accuracy in tracking the gripper's centroid of 106 ± 30 μm. Similar subjective evaluation approaches are quite common in the literature [31], [32].

D. Control

1) Motion control: The magnetic field strength ($\mathbf{B}(\mathbf{P})$) can be determined by superposition of each individual electromagnet:

$$\mathbf{B}(\mathbf{P}) = \sum_{i=1}^{e} \mathbf{B}_i(\mathbf{P}) \tag{23}$$

where e is the number of electromagnets within the magnetic system. The magnetic field generated by the i_{th} electromagnet is linearly proportional to the current (I_i) through the electromagnet:

$$\mathbf{B}_i(\mathbf{P}) = \tilde{\mathbf{B}}_i(\mathbf{P}) I_i \tag{24}$$

where $\tilde{\mathbf{B}}_i(\mathbf{P}) \in \mathbb{R}^{3\times 1}$ depends on the position at which the magnetic field is evaluated. $\tilde{\mathbf{B}}_i(\mathbf{P})$ is determined in previous studies using a finite element model and experimentally verified using a calibrated three-axis Hall magnetometer [2]. Combining Equations (23) and (24) yields

$$\mathbf{B}(\mathbf{P}) = \sum_{i=1}^{e} \tilde{\mathbf{B}}_i(\mathbf{P}) I_i = \tilde{\mathbf{B}}(\mathbf{P})\mathbf{I} \tag{25}$$

where $\mathbf{I} \in \mathbb{R}^{6\times 1}$ is the vector of applied currents through the electromagnets. The magnetic force can now be

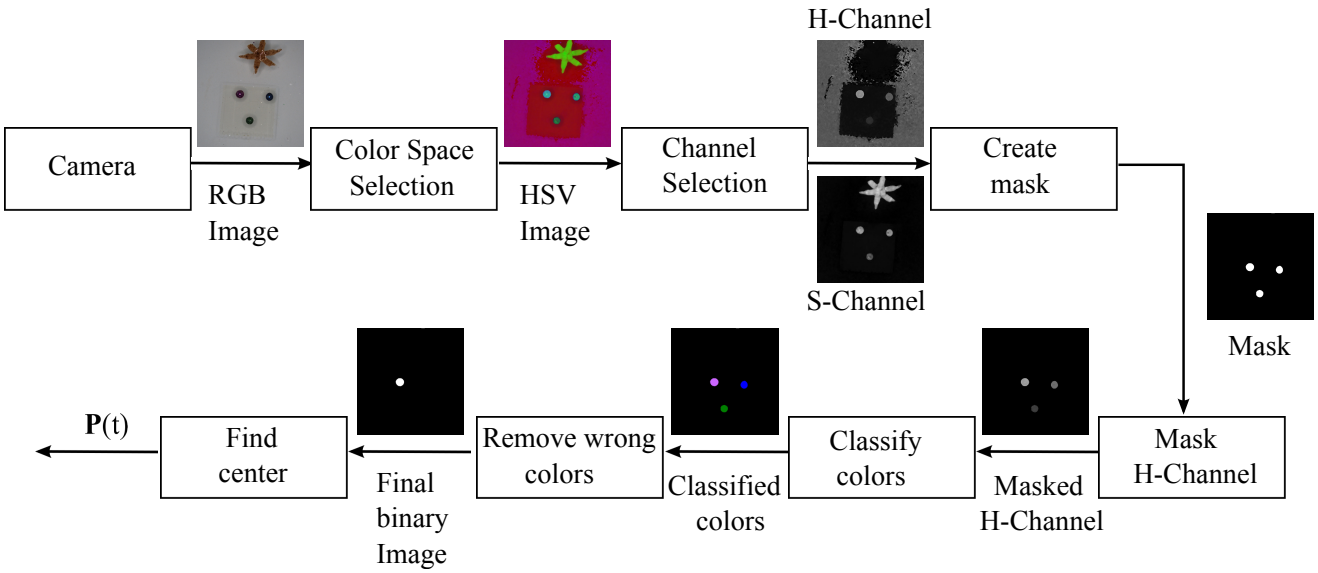

Fig. 8: Microbead tracking algorithm. Each frame registered by the high-resolution camera is first converted to HSV colorspace. From the HSV colorspace the hue (H) and saturation (S) channel are extracted. The S-channel is used to create a mask using an adaptive threshold and removing small and large blobs. The mask is used to extract the microbead location in the H-channel of the image. From the H-channel the bead colors are classified and then wrong colors are removed from the binary image. The end result is an binary image containing only the microbead which has the color of interest. From this image the center of the microbead is found in the same manner as for gripper tracking.

computed by combining Equations (4) and (25):

$$\mathbf{F}(\mathbf{P}) = \Lambda(\mathbf{m}, \mathbf{P})\mathbf{I}, \tag{26}$$

where $\Lambda(\mathbf{m}, \mathbf{P}) \in \mathbb{R}^{3\times 6}$ is the actuation matrix of the magnetic system given by

$$\Lambda(\mathbf{m}, \mathbf{P}) = \mathbf{m}(\mathbf{P})\nabla\tilde{\mathbf{B}}(\mathbf{P}) \tag{27}$$

The magnetic dipole moment of the gripper ($\mathbf{m}(\mathbf{P})$) is determined experimentally (Sec. IV-F.1) and can be found in Sec. V-A.

The desired magnetic force is calculated using a PID-controller:

$$\mathbf{F}(\mathbf{P}) = \mathbf{K_p}\mathbf{e} + \mathbf{K_i}\int_{t_0}^{t_f} \mathbf{e}\ dt + \mathbf{K_d}\dot{\mathbf{e}}, \tag{28}$$

where $\mathbf{K_p} \in \mathbb{R}^{3\times 3}$, $\mathbf{K_i} \in \mathbb{R}^{3\times 3}$ and $\mathbf{K_d} \in \mathbb{R}^{3\times 3}$ are positive definite matrices representing the proportional, integral, and derivative gain of the PID-controller given by

$$\mathbf{K_p} = \begin{bmatrix} K_{p1} & 0 & 0 \\ 0 & K_{p2} & 0 \\ 0 & 0 & K_{p3} \end{bmatrix}, \mathbf{K_i} = \begin{bmatrix} K_{i1} & 0 & 0 \\ 0 & K_{i2} & 0 \\ 0 & 0 & K_{i3} \end{bmatrix},$$
$$\mathbf{K_d} = \begin{bmatrix} K_{d1} & 0 & 0 \\ 0 & K_{d2} & 0 \\ 0 & 0 & K_{d3} \end{bmatrix} \tag{29}$$

Furthermore in Equation (28) $\mathbf{e} \in \mathbb{R}^{3\times 1}$ is the setpoint-error given by

$$\mathbf{e} = \mathbf{P_{ref}} - \mathbf{P} \tag{30}$$

where $\mathbf{P_{ref}} \in \mathbb{R}^{3\times 1}$ is the reference position of the gripper. The desired current is found by combining Equations (26) and (28):

$$\mathrm{I} = \Lambda^{\dagger}\mathbf{F}(\mathbf{P}) = \Lambda^{\dagger}[\mathbf{K_p}\mathbf{e} + \mathbf{K_i}\int \mathbf{e}\ dt + \mathbf{K_d}\dot{\mathbf{e}}], \tag{31}$$

where † is the symbol for pseudo-inverse. The parameters of the PID-controller were tuned using Ziegler-Nichols method [33]. The desired current is sent to Elmo Whistle servo controllers which control the currents through the electromagnets. For this study we only have position feed back in x- and y-direction of the grippers. The z-position is controlled by applying either maximum force in the positive z-direction, maximum force in the negative z-direction of the gripper or no force in z-direction at all.

2) Temperature control: In order to automatically open and close the grippers the temperature of the water in the petri dish is controlled by a Peltier element connected to an Arduino Uno. We choose a Peltier element as heating element because by reversing the current a Peltier element can also be used to cool off the water. The voltage across the plates of the Peltier element is determined by

$$U = K_{pT}(T_{des} - T_{curr}) \tag{32}$$

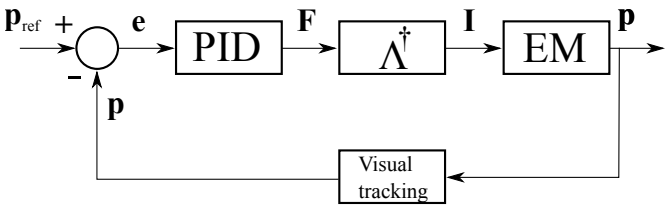

Fig. 9: Control loop for the magnetic system. Here PID represents the controller of the system, Λ is the actuation matrix that maps the desired magnetic force $\mathbf{F}$ into the currents $\mathbf{I}$ supplied to the electromagnets EM. † is the symbol for pseudo-inverse. $\mathbf{P}_{ref}$ and $\mathbf{P}$ are the reference position and gripper position, $\mathbf{e}$ is the positioning error. Furthermore the visual tracking block represents the camera and tracking system.

where K_{pT} is the proportional gain, T_{des} is the desired temperature, T_{curr} is the current temperature measured by the temperature probe and U is the voltage over the Peltier element powered by the Arduino Uno microcontroller.

3) Autonomous pick-and-place: As will be explained in Sec. IV-F.5 for this work the grippers are employed to sort micro-beads of different colors autonomously. The autonomous pick-and-place operation combines all tracking, motion control and temperature control steps described in the previous sections. Fig. 10 shows the flowchart of the autonomous pick-and-place operation. The remainder of this section will go into more detail of the individual steps of the flowchart.

When the autonomous pick-and-place operation starts the micro-bead tracking algorithm as explained in Sec. IV-C.7 is ran and the number of beads is counted. Every time a micro-bead is successfully delivered a bead counting variable is increased by one. Once the bead counting variable reaches the number of beads counted at the start all micro-beads are placed, the autonomous pick-and-place operation ends and the gripper returns to the center of the workspace as can be seen in the flowchart. If not all micro-beads are placed the algorithm proceeds with color selection as can be seen from the flowchart. The color of interest is selected and the other colors are removed from the binary image as explained in Sec. IV-C.7. The flowchart shows an example binary image after color selection. From this binary image the center of the micro-bead is extracted and passed to the gripper as setpoint. When all beads of a certain color are pick-and-placed the color of interest is changed for the next cycle. The moment the gripper approaches a micro-bead and gets into a certain radius the upper electromagnet is activated to pull the gripper up in z-direction to get on top of the micro-bead. Once the gripper is on top of the micro-bead the the water in the petri dish is heated and the gripper closes. When the gripper is recognized as closed (explained in Sec. IV-C) the motion controller gains are changed and the gripper is moved away from its location towards the drop off point. After the gripper leaves an area of a certain radius from the micro-bead location, the micro-bead tracking algorithm is run again to count the number of micro-beads. If the number of micro-beads is decreased by one it means the gripper has grabbed the micro-bead and the gripper continues moving towards the drop off location. If the number of micro-beads did not decrease the water in the petri dish gets cooled off. Once the gripper is recognized as open it will approach the micro-bead again. When the micro-bead is grabbed and the gripper arrives at the drop off location the water cools off and the micro-bead is placed when the gripper is open. After the micro-bead is placed the above steps will be repeated until all micro-beads are placed.

E. Path planning

For this study grippers are also employed to retrieve biological tissue while avoiding obstacles. Obstacle avoidance can be achieved with the use of a path planner. Path planners partition the world into a structure which reduces the number of dimensions that a planner has to deal with. The elements of such a structure are the states of the path planner and they are used to generate obstacle-free paths. Let $\mathcal{C}$ be the configuration space, i.e. the space of all possible displacements of the moving object and let $\mathcal{F}$ be the free space (a collision-free subset of $\mathcal{C}$).

There are multiple types of path planners but for the gripper experiments of this study a probabilistic planner is used. Probabilistic planners represent a class of methods of remarkable efficiency, especially in problems involving high-dimensional configuration spaces. The

Algorithm 1 RRT is a tree $\mathcal{T}$ rooted at the gripper's initial state $\mathbf{x}_{start}$. At each iteration, a new state $\mathbf{x}_{sample} \in \mathcal{F}$ is sampled, and a feasible control that grows $\mathcal{T}$ toward the sampled state is computed. The output of the RRT is a motion plan where T is the number of steps.

```
1: function BUILD_RRT
2:     T ← x_start;
3:     for k = 1 to T do
4:         x_sample ← RANDOM_STATE(F);
5:         x_nn ← NEAREST_NEIGHBOUR(T, x_sample);
6:         (x_new, f) ← CONNECT(x_nn, x_sample);
7:     end for
8:     return [(x_start, f_start), ..., (x_T, f_T)];
9: end function
```

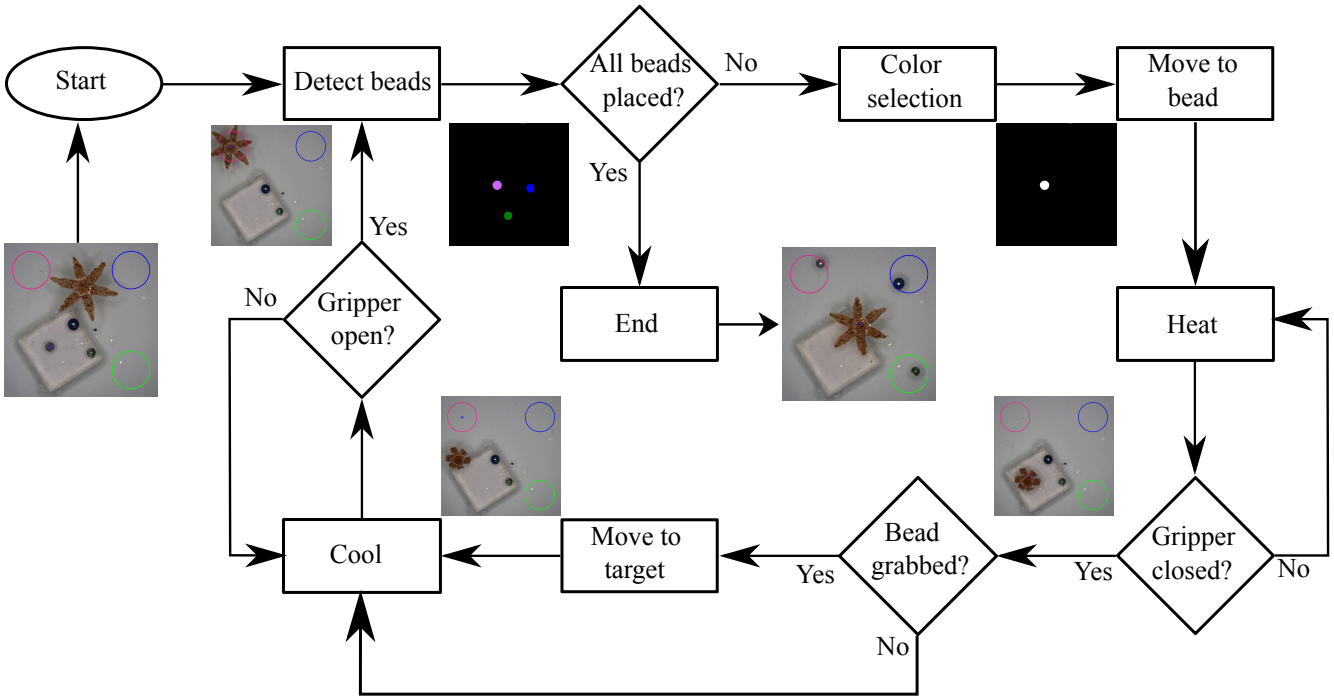

Fig. 10: Flowchart of the autonomous pick-and-place operation. For the autonomous pick-and-place operation the tracking, motion control and temperature control steps described in the previous sections are combined. The blocks shown in this flowchart are the basic steps and are explained more elaborately in this section.

downside of the probabilistic methods is that they are only probabilistically complete, i.e., the probability of finding a solution to the planning problem when one exists tends to 1 as the execution time tends to infinity. This means that, if no solution exists, the algorithm will run indefinitely. In practice, a maximum number of iterations is enforced so as to guarantee its termination.

For the obstacle avoidance experiments of this work we selected the rapidly exploring random tree (RRT) algorithm for path planning. The RRT is a tree $\mathcal{T}$ rooted at the gripper's initial state $\mathbf{x}_{start}$. At each iteration, the algorithm samples a state $\mathbf{x}_{sample} \in \mathcal{F}$, finds its nearest neighbors $\mathbf{x}_{nn}$ in the tree, and computes a feasible control $\mathbf{f}$ that grows the tree toward the sampled state [34], [35]. The tree is grown toward the sampled state by applying the control input $\mathbf{f}$ to the dynamic model of the gripper. The output of the RRT is a motion plan [($\mathbf{x}_{start}$, $\mathbf{f}_{start}$), ..., ($\mathbf{x}_T$, $\mathbf{f}_T$)], where T is the number of steps (see Algorithm 1). The most important advantages of RRTs is that they can deal with real-valued spaces of extremely high dimension and they can handle dynamics.

For the experimental work, we used a standard RRT-GoalZoom policy [35] where the new random state is generated based on a biased coin toss that chooses a random sample from either a region around the goal or the whole space. Instead of extending an RRT by an incremental step, we iterated until the random state or an obstacle is reached. Moreover, we used a fixed planning time interval of $T = 0.1$ s. At the beginning the RRT computes the motion plan. Then, for each period of duration T, the system executes the previously computed plan and simultaneously the motion planner computes an updated plan that will be ready for the next time interval.

F. Experimental plan

In order to characterize the grippers and show the performance of both the grippers and the experimental set-up for different tasks we conducted the following experiments:

- Motion control experiments.
- Thermal and magnetic characterization of the grippers.
- Pick-and-place of micro sized beads.
- Pick-and-place of biological tissue with obstacle avoidance.
- Autonomous sorting of colored beads.
- Haptic experiments.

The above experiments are described into more detail in the remainder of this section. Sec. V will show the results of the experiments.

1) Gripper characterization: The grippers are characterized both thermally and magnetically. For the thermal characterization the temperature of the water is increased

until the gripper fully closes, and then decreased to room temperature so that the gripper opens again. During this procedure the gripper changes its configuration from star-shaped to circular, and back. The configuration is analyzed by a dimensionless metric C which relates the temperature depended perimeter length of the gripper $P(T)$ to its maximum P_{max} minimum P_{min} perimeter length. C is observed by the tracking system during heating and cooling of the water and is given by:

$$C = \frac{P(T) - P_{min}}{P_{max} - P_{min}}. \tag{33}$$

Thermal characterization of the grippers is executed by opening and closing 3 different grippers for 5 cycles.

The grippers are magnetically characterized by determining their magnetic dipole moment. The magnetic dipole moment of the grippers ($\mathbf{m}_{mg} \in \mathbb{R}^{3\times1}$) is required for modeling purposes. We need it to calculate the actuation matrix Λ of the system. The actuation matrix is used to map the applied currents through the electromagnets into the magnetic force acting on the grippers as discussed in Sec. IV-D. The magnetic dipole moment can be calculated as the volume integral of the induced magnetization ($\mathbf{M}(\mathbf{P})$) [36]

$$\mathbf{m}(\mathbf{P}) = \int_V \mathbf{M}(\mathbf{P}) dV \tag{34}$$

where V is the volume of the gripper. Since the complex shape of the grippers we decided to determine the magnetic dipole moment experimentally. In order to do so we assume the gripper to have uniform iron-oxide distribution and we divide the six-tip gripper in three pairs of counter-posed two-tip dipoles. The magnetic dipole moments of the latter ones ($\mathbf{m}_{tips} \in \mathbb{R}^{3\times1}$) can be superposed to obtain $\mathbf{m}_{mg}$ (Fig. 11). The magnetic dipole moment of these two-tip dipoles ($\mathbf{m}_{tips}$) can be experimentally measured. By applying a magnetic field the two-tip dipoles will align along the magnetic field lines and move along the gradient. Reversing the field direction causes them to change direction and make a u-turn with diameter (D) given by [37]:

$$D = \frac{\alpha\pi|\dot{\mathbf{P}}|}{|\mathbf{m}||\mathbf{B}(\mathbf{P})|} \tag{35}$$

where $\dot{\mathbf{P}} \in \mathbb{R}^{3\times1}$ and $\mathbf{m}$ are the linear velocity and the magnetic dipole moment of the dipole, and α is its rotational drag coefficient. We estimated α to be 2.2×10^{-11} Am^{2}sT by approximating the two-tips dipole with a cylinder [38]. In order to initiate the required u-turns we apply uniform magnetic fields of 3.5 mT and reverse the fields. The experiment is repeated 20 times and use the average u-turn diameter (D) and velocity to determine the magnetic dipole moment of the grippers.

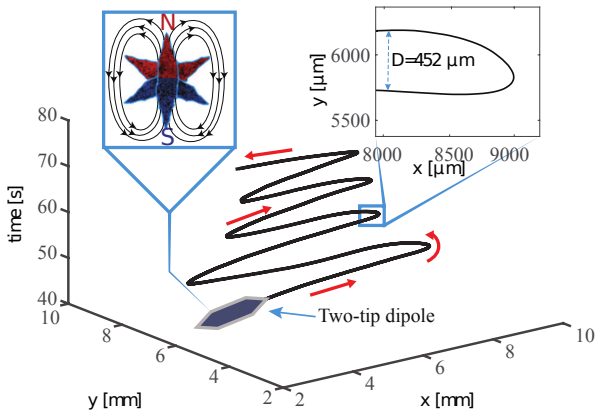

Fig. 11: Schematic of the trajectory of the two-tip dipole during the *U-turn experiments* for magnetic characterization. *Left inset:* A graphical representation of the magnetic dipole moment of the soft gripper as superposition of the magnetic dipole moments of its two-tip dipoles.

2) Motion control experiments: Motion control experiments are executed to evaluate the performance of the experimental system and the grippers. The experiments will show that the system is capable of precisely controlling the gripper's motion for point-to-point control and tracking of a circular and square path. The circular path has a radius of 3 mm and the square path has sides of 6 mm. For the point-to-point control experiments 5 randomly assigned points in the workspace are chosen. The motion control experiments are carried out for both loaded and unloaded grippers. The loaded grippers carry a 500 μm micro-bead. From the experiments the following metrics will be evaluated:

- Average velocity.
- Trajectory error.
- ROC (Region of convergence).

The trajectory error is defined as the average difference between the desired trajectory and the actual path of the grippers evaluated at 500 points of the trajectory. The ROC is defined as the radius of the neighborhood around the setpoint in which the gripper stays with the point-to-point experiments. In order to achieve statistically reliable results we used 10 grippers which each completed 5 trials of the three described experiments for a total of 50 trials per experiment.

3) Pick-and-place experiment: The benefit of grippers above previously researched micro-robots is their ability to grab and release objects. Therefore for this study the grippers are employed to perform a pick-and-place task. In order to demonstrate the gripper's grabbing dexterity and the accuracy of the experimental set-up a 500 μm sized micro-bead is transported from one random location in the workspace to another random location in the workspace.

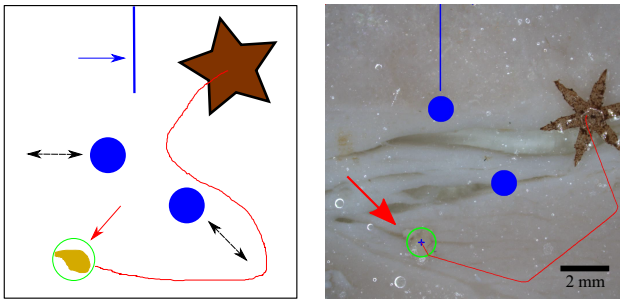

(a) (b)

Fig. 12: (a) Sketch of the pick-and-place experiment with obstacle avoidance. The blue arrow shows the static obstacle, the black arrows show the dynamic obstacles with their direction of motion and the red arrow shows the piece of biological material which has to be picked up. Furthermore the red line shows a possible trajectory for the gripper to reach the biological material. The static obstacle is a wall of dimensions 10×3500 μm and dynamic obstacles are circles with radius 500 μm. One dynamic obstacle only moves in x-direction with velocity 300 μm/s. The other dynamic obstacle moves diagonally with a velocity of 300 μ/s in both x- and y-direction. (b) A snapshot of the experiment during a representative experiment. Also in this snapshot the red arrow points out the piece of biological material and the red line shows the computed path by the path planner.

This experiment is performed 5 times and the results are evaluated based on the following metrics:

- Average drop off error.
- Average execution time.
- Average velocity.

The drop off error is defined as the distance between the center of the micro-bead and the drop off location. The average velocity is defined as the average velocity of the gripper with payload.

4) Pick-and-place of biological tissue in a dynamic and cluttered environment: The soft property of the grippers makes it possible to handle biological tissue without damaging it. This makes the grippers very suited for retrieving tissue samples from the human body such as with a biopsy operation. For reliable results of a biopsy operation it is very important that the physician can retrieve tissue without damaging it. Also the grippers could potentially be employed for endarterectomies. In order to show the potential of the grippers for both these medical applications for this experiment the grippers will pick-and-place chicken-egg yolk without damaging it. Egg yolk was chosen for its high content of low-density lipoprotein (LDL). This makes the consistency of the yolk very similar to one of the plaques that are removed in endarterectomies. In order to increase resemblance between the experimental scenario and the human body the task is completed on base of porcine muscular tissue.

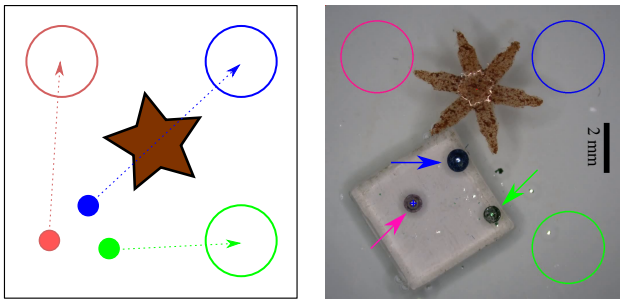

(a) (b)

Fig. 13: (a) A schematic drawing of the autonomous pick-and-place experiment. The sketch the 3 different colored micro-beads with arrows pointed to their drop off locations. (b) A snapshot of the start of the experiment. The pink, blue and green arrows in this picture show the beads of the same color. The colored circles have radius 1500 μm and represent the drop off locations of the beads. The grippers should recognize the micro-bead colors and drop them off at their respective drop off locations

During the pick-and-place task the gripper has to avoid one static and two dynamic obstacles. The dynamic obstacles are circles of radius 500 μm. One dynamic obstacle only moves in x-direction with velocity 300 μm/s. The other dynamic obstacle moves diagonally with a velocity of 300 μ/s in both x- and y-direction. The static obstacle is a wall with dimensions 10×3500 μm. All obstacles are virtual. For this experiment the grippers will start at the top right of the workspace to pick up the biological material from the bottom left of the workspace approximately 1.5 cm from its starting. The egg yolk will be released at the top right of the workspace after which the gripper returns to the bottom left of the workspace. During this experiment the radius of the gripper which is used for the obstacle avoidance algorithm is adjusted for open and closed grippers. Fig. 12 shows a schematic overview of the experiment.

The results of this experiment are evaluated based on the following metrics:

- Average velocity.
- Average drop off error.
- Average execution time.

The average velocity is computed both for loaded and unloaded grippers separately. The drop off error is defined as the distance between the center of the egg yolk and the drop off position.

5) Autonomous micro-bead sorting experiment: The micro-bead pick-and-place experiment showed the system's and gripper's capabilities to precisely pick-and-place micro-beads. Driven by the increasing demand in automation we will employ the grippers for autonomous sorting of different colored beads. This experiment also

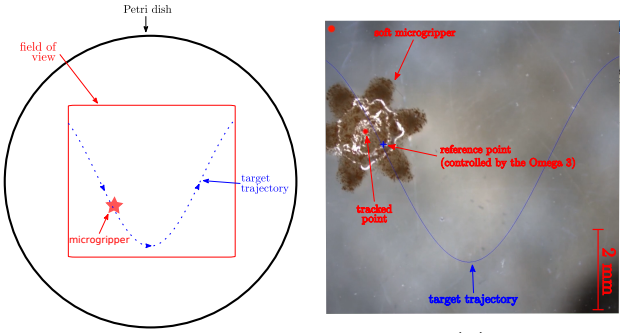

(a) (b)

Fig. 14: Experiment #1: Path following task. Subjects are required to steer a gripper along the predetermined trajectory, being as fast and precise as possible. We considered four target trajectories and eight feedback conditions.

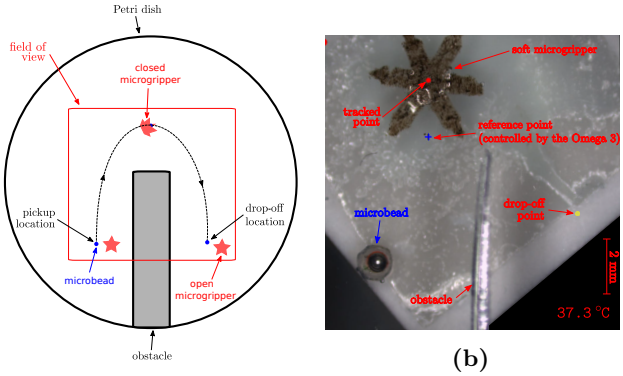

(a) (b)

Fig. 15: Experiment #2: Pick-and-place task. The task consists of picking up a microbead from the ground and dropping it off at a predetermined location. Subjects are able to move, close, and open the gripper through the haptic interface. Moreover, through the same interface, they receive haptic feedback about the interaction of the gripper with the environment.

shows proof of concept for recognition of light-colored plaque as discussed for the previous experiment. For this experiment 3 beads of different color are placed in the workspace. The beads each have their own drop off location: a circle of radius 1500 μm of the same color. The gripper will autonomously sort the 3 micro-beads by picking them up and placing them at their drop off location. After the last bead is dropped off the gripper will return to a neutral position. During this experiment the gripper's configuration is used as feedback to control the temperature of the water. The choice for this feedback over temperature measurements was made taking into account issues related to positioning a temperature sensor inside a blood vessel. Fig. 13 shows a sketch and snapshot of the experiment. In order to evaluate the results of this experiment the following metrics will be computed based on 5 experiments:

- Average drop off error.
- Average execution time.
- Average velocity.

The drop off error is defined as the distance between the center of the micro-bead and the center of its drop off circle right after the bead was dropped off. The average velocity is taken for gripper with and and without payload.

6) Haptic experiments: In addition to the previously explained experiments we experimented with the use of haptics to control the grippers. As it takes time for people to accept autonomously operating micro-robots inside their body the use of haptics might be a good first step towards autonomous surgery. We carried out two types of experiments: the first experiment focuses on the result of haptic feedback on motion control of the grippers, the second experiment focuses on the results of haptic feedback on a simple pick-and-place operation. During these experiments which are explained into more detail in the remainder of this section we consider different types of haptic feedback. The results are evaluated using volunteers.

In order to understand the role of haptic feedback for the control of grippers we carried out two sets of experiments.

- Evaluation of the steering capabilities of the system for a path following task.
- Evaluation the steering capabilities of our system for a pick-and-place task.

For both experiments participants were briefed about the task and afterward signed an informed consent, including the declaration of having no conflict of interest. All of them were able to give the consent autonomously. The participation in the experiment did not involve the processing of genetic information or personal data (e.g., health, sexual lifestyle, ethnicity, political opinion, religious or philosophical conviction), neither the tracking of the location or observation of the participants. Our organization does not require any IRB review for this case.

The experimenter explained the procedures and spent about three minutes adjusting the setup to be comfortable before the subject began the experiment. No practice trial was allowed.

For experiment 1 sixteen subjects (14 males, 2 female, age range 22 - 31 years) took part in the experiment, all of whom were right-handed. Six of them had previous experience with haptic interfaces.

For experiment 2 Ten subjects (9 males, 1 female, age range 24 - 33 years) took part in the experiment, all of whom were right-handed. Five of them had previous experience with haptic interfaces. None of all subjects

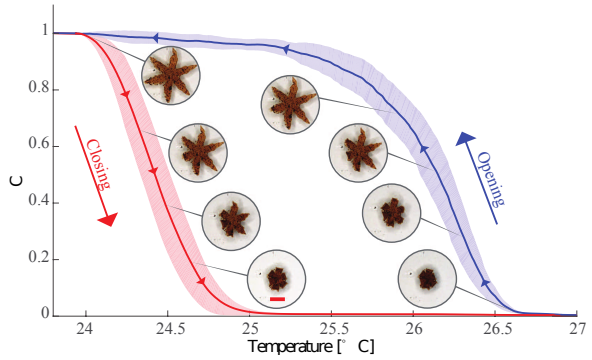

Fig. 16: Results of of the opening and closing characterization of the grippers. The red line and its corresponding shade show the average configuration (C) with standard deviation of the grippers when heating the water in the petridish. The blue line and its corresponding shade show the same for cooling. The values in this figure are computed from a total of 15 opening and closing cycles. The gripper configuration is given by $C = \frac{P(T)-P_{min}}{P_{max}-P_{min}}$ where $P(T)$ is the length of the contour of the gripper at temperature T. P_{max} and P_{min} are the gripper's maximum (open) and minimum (closed) perimeter length.

reported any deficiencies in their perception abilities. Both experiments lasted approximately 30 minutes.

A sketch of the first experiment can be seen in Fig. 14a. The task consisted of steering a gripper in the remote environment along a predetermined trajectory, being as fast and precise as possible. According to the feedback condition considered, the subject is provided with visual, kinesthetic, frictional, or vibrotactile feedback about the error in following the target trajectory (see below). We considered four different trajectories,

1) $y = 13.6 - 3.2\sin\left(\frac{\pi}{6} - \frac{x}{2}\right)$,
2) $y = 13.6 - 3.2\sin\left(\frac{7\pi}{6} - \frac{x}{2}\right)$,
3) $y = 13.6 - 3.2\sin\left(\frac{\pi}{6} - x\right)$,
4) $y = 13.6 - 3.2\sin\left(\frac{7\pi}{6} - x\right)$.

We considered eight different feedback conditions, that are combinations of these four types of feedback: visual feedback (Vs), kinesthetic feedback (K), vibrotactile feedback (Vb), frictional feedback (Pc), and inertia (I). When visual feedback is provided, the target trajectory is simply shown on the screen (as in Fig. 14b).

When kinesthetic feedback is provided, the Omega interface provides an attractive kinesthetic force that keeps the user close to the target trajectory. This force $\mathbf{f_k}(\mathbf{t}) \in \mathbb{R}^2$, provided by the Omega along its x and y axes, is given by

$$\mathbf{f_k}(\mathbf{t}) = -k_k(\mathbf{p_r}(\mathbf{t}) - \mathbf{p_{t,r}}) - b_k\dot{\mathbf{p}}_\mathbf{r}(\mathbf{t}), \qquad (36)$$

where $k_k = 1000$ N/m, $b_k = 5$ Ns/m, $\mathbf{p_r}(\mathbf{t}) \in \mathbb{R}^2$ is the current position of the reference point as controlled by the user through the haptic interface, and $\mathbf{p_{t,r}}$ is the point on the target trajectory closest to $\mathbf{p_r}(\mathbf{t})$.

When vibrotactile feedback is provided, the Omega provides a vibration as soon as the user moves the end-effector out from the target trajectory. The amplitude of the vibration increases as the end-effector of the Omega moves away from the target trajectory. This force $\mathbf{f_{vb}}(\mathbf{t}) \in \mathbb{R}^2$, provided by the Omega along its x and y axes, is

$$\mathbf{f_{vb}}(\mathbf{t}) = k_{vb}(\mathbf{p_r}(\mathbf{t}) - \mathbf{p_{t,r}}) \begin{bmatrix} \sin(2\pi f_{vb}t) \\ \sin(2\pi f_{vb}t) \end{bmatrix}, \qquad (37)$$

where $k_{vb} = 50$ N/m and $f_{vb} = 150$ Hz. The frequency of the vibration has been chosen to maximally stimulate the Pacinian corpuscle receptors [39] and fit the master device specifications.

When frictional feedback is provided, the Omega increases its friction when the user moves the reference point away from the target trajectory. This force $\mathbf{f_{pc}}(\mathbf{t}) \in \mathbb{R}^2$, provided by the Omega along its x and y axes, is

$$\mathbf{f_{pc}}(\mathbf{t}) = \begin{cases} -b_{pc}\dot{\mathbf{p}}_\mathbf{r}(\mathbf{t}) & \text{if moving away from the target trajectory,} \\ 0 & \text{otherwise,} \end{cases} \qquad (38)$$

where $b_{pc} = 20$ Ns/m.

Finally, when feedback about the inertia of the gripper is provided, the Omega provides an attractive kinesthetic force that keeps the reference point close to the controlled gripper. This force $\mathbf{f_i}(\mathbf{t}) \in \mathbb{R}^2$, provided by the Omega along its x and y axes, is

$$\mathbf{f_i}(\mathbf{t}) = -k_i(\mathbf{p_r}(\mathbf{t}) - \mathbf{p_m}(\mathbf{t})), \qquad (39)$$

where $k_i = 200$ N/m, and $\mathbf{p_m}(\mathbf{t}) \in \mathbb{R}^2$ is the current position of the gripper as evaluated by the tracking system.

We combined the abovementioned types of feedback in four conditions:

1) Visual feedback (Vs),
2) Visual feedback + Vibrotactile feedback (Vs + Vb),
3) Visual feedback + Frictional feedback (Vs + Pc),
4) Kinesthetic feedback (K),

and we tested all these conditions with and without providing feedback about the inertia of the gripper, ending up with 4 (feedback conditions) × 2 (with and without inertia) × 4 (target trajectories) = 32 different experimental conditions.

Visual feedback on the remote environment is always provided to the subjects through the high-resolution camera, and the Omega 6 haptic interface is always used to provide the controller with the gripper's reference point. The passivity algorithm presented by [40] guarantees the

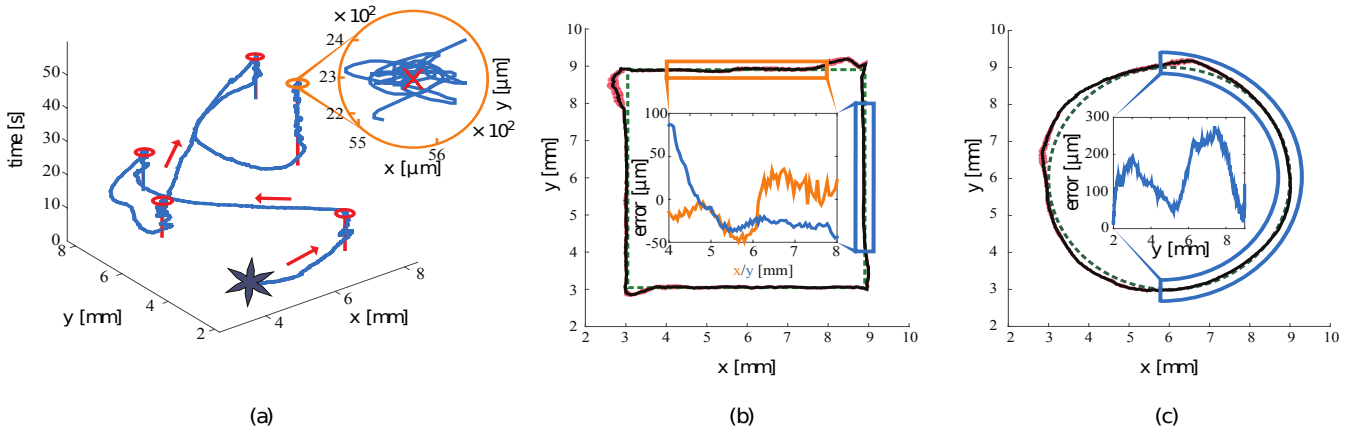

Fig. 17: Closed-loop motion control experimental results of the grippers. (a) An example of point-to-point motion control experiments. The red lines represents the setpoint, the blue line the trajectory of the gripper, and the red circles the ROC. (b) and (c) depict the results of the trajectory following experiments. The green dashed path represents the reference trajectory, the black line shows the path of the grippers, and the red area represents the standard deviation for the corresponding point among all the performed experiments. The insets show the positioning error in the highlighted parts of the trajectories. The results are based on 50 trials in total

stability of the control loop (see Section IV-D). The environment variables defined in Equations. (36)-(39) have been selected by carrying out a pilot experiment enrolling three subjects (3 males, age range 21 - 32 years), who did not participate in the main experiment described in this section. They were asked to interact with the environment and modify at runtime the values of the considered variables (i.e., k_k, b_k k_{vb}, k_i, b_{pc}, and k_i) until the haptic interaction felt as natural as possible. In this experiment the temperature of the remote environment was fixed to keep the controlled gripper always open.

The second haptic experiment aims at evaluating our teleoperation system in a pick-and-place task, as sketched in Fig. 15a. The task consists of picking up a polystyrene micro-bead from the ground and dropping it off at a predetermined location. An obstacle is placed in the middle of the remote environment (see Fig. 15b). The pick up and drop-off locations were chosen randomly in the left and right hand sides of the environment, respectively. The micro-bead was placed on a small pedestal to make the pick up easier.

Each subject made six randomized repetitions of the pick-and-place task, with two repetitions for each feedback condition proposed:

- Kinesthetic feedback + Inertia (K + I), where kinesthetic force is used to render both the inertia of the controlled gripper and the collisions between the reference point and the obstacle.
- Vibrotactile feedback + Inertia (V + I), where kinesthetic force is used to render the inertia of the controlled gripper and vibrotactile feedback is used to render the collisions between the reference point and the obstacle.
- No force feedback (N).

In condition K+I, the Omega haptic interface provides the subject with kinesthetic feedback about the collisions of the reference point with the obstacle and about the inertia of the gripper. Kinesthetic feedback $\mathbf{f_{k,2}(t)}$, responsible for rendering collisions of the reference point with the obstacle, is evaluated according to the popular god-object model [41], and the obstacle is modeled as a spring-damper system:

$$\mathbf{f_{k,2}(t)} = -k_{k,2}(\mathbf{p_r(t)} - \mathbf{p_{r,proxy}(t)}) - b_k\dot{\mathbf{p}}_\mathbf{r}(\mathbf{t}). \quad (40)$$

$k_{k,2} = 1000$ N/m, $b_k = 5$ Ns/m, $\mathbf{p_r(t)} \in \mathbb{R}^2$ is the current position of the reference point as controlled by the subject through the haptic interface, and $\mathbf{p_{r,proxy}(t)} \in \mathbb{R}^2$ is the virtual location of the haptic interface, placed where the haptic interface point would be if the haptic interface and the object were infinitely stiff (i.e., on the surface of the obstacle in our case) [41]. On the other hand, kinesthetic feedback $\mathbf{f_i(t)}$, responsible for rendering the inertia of the gripper, is evaluated as in Equation (39). In this condition the subject feels an opposite force when trying to penetrate the obstacle and when moving the reference point away from the gripper.

In condition V+I, the Omega haptic interface provides the subject with vibrotactile feedback about the collisions of the controlled gripper with the obstacle and kinesthetic feedback about the inertia of the gripper. Vibrotactile feedback $\mathbf{f_{vb,2}(t)}$ is evaluated according to the god-object model, and the obstacle is modeled as a spring system:

$$\mathbf{f_{vb}(t)} = k_{vb}(\mathbf{p_r(t)} - \mathbf{p_{r,proxy}(t)}) \begin{bmatrix} \sin(2\pi f_{vb} t) \\ \sin(2\pi f_{vb} t) \end{bmatrix}, \quad (41)$$

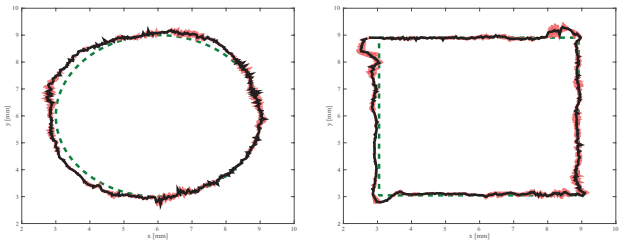

Fig. 18: Closed-loop motion control experimental results of the closed gripper. (a) shows the circle trajectory following experiment (b) depicts the square trajectory following experiment. The green dashed path represents the reference trajectory, the black line shows the path of the gripper, and the red area represents the standard deviation for the corresponding point among all the performed experiments. The results are based on 5 trials in total

where $k_{vb} = 80$ N/m and $f_{vb} = 150$ Hz. The inertia is again rendered as in Equation (39). In this condition the user feels a vibration every time that the reference point enters in contact with the obstacle. Moreover, as in condition K+I, the user feels an opposite force when moving the reference point away from the gripper.

In condition N, the system provides no information about the inertia of the gripper and the collisions between the controlled gripper and the obstacle.

In all three conditions, the closing and opening of the gripper is managed by controlling the temperature level of the remote environment through the Peltier element. The target temperature is set by rotating the pen-shaped end-effector of the Omega interface, as detailed in Sec. IV-A.2. Visual feedback on the remote environment is always provided to the subjects through the high-resolution camera, and the Omega 6 haptic interface is always used to provide the controller with the gripper's reference point. The passivity algorithm presented by [40] guarantees again the stability of the control loop. The considered environment variables (i.e., $k_{k,2}$, b_k, and k_{vb}) have been selected by carrying out a pilot experiment analogous to the one described for experiment 1.

V. Experimental results

This section will show the results of the experiments described in Sec. IV-F. The results of each experiment will be described shortly in its own subsection. TABLE shows an overview of the results of all experiments?

A. Gripper characterization

1) Magnetic dipole moment: As told in the experimental plan to determine the magnetic dipole moment of the grippers ($\mathbf{m}_{mg}$) we need the average *U-turn* diameter and velocity. Based on 20 experiments the we measured the average *U-turn* diameter and velocity to be 193 μm and 739 μm/s, respectively. Using Equation (35) we obtain $|\mathbf{m}_{tips}| = 3.5\times10^{-8}$ Am^2. The direction of $\mathbf{m}_{tips}$ is determined using $\mathbf{m}_{tips} = p\mathbf{d} = |\mathbf{m}_{tips}|\frac{\mathbf{d}}{|\ell|}$ where $p \in \mathbb{R}$ is the magnetic pole strength and $\mathbf{d} \in \mathbb{R}^{3\times1}$ is the vector separating the two poles. Finally, the magnetic dipole moment of the gripper is computed as the superposition of three rotated two-tip dipoles.

We note that the adopted technique overestimates the magnetic dipole moment of the central overlapping part. However, this section is assumed to have a negligible effect on the overall magnetic dipole moment due to its small $\mathbf{d}$.

2) Thermal characterization: The gripper configuration metric C(Equation (33)) is analyzed for five successive opening and closing cycles for three different grippers. The grippers on average completely opened at temperatures below 24 °C and fully closed above 27 °C. However, we noticed a variance of these boundaries depending on the temperature dynamics. Open grippers closed at lower temperatures than the ones at which closed grippers opened. This advantageous behavior makes the grippers more responsive to thermal control actions. The observed gripper configuration metric C is plotted against temperature and can be seen in Fig. 16.

B. Motion control experiments

In these experiments we evaluated closed-loop control of the grippers during point-to-point control and tracking of circular and square paths (Fig. 17). The grippers without payload moved with an average velocity and positioning error of 721±132 μm/s and 115±104 μm, respectively. The experimental results are tabulated in Table I. The average positioning error for the 150 experimental trials is 3% of the body length of the gripper. The error never reaches values above 5.5% of the gripper body length and such errors only occur during sharp turns, when the magnetic dipole moment of the gripper and the magnetic field are the least aligned, resulting in a weaker magnetic force (Equation (4)).

From Fig. 17 we noticed that the difference in motion between the grippers is very small. In order to determine whether this difference can be considered statistically negligible, we used the two one-sided t-test approach (TOST) [42], [43]. The null hypothesis of the TOST states that the mean values of two groups are different by at least a certain amount ε. Then, in order to test for equivalence, the 90% confidence intervals for the difference between the two groups are evaluated. The null hypothesis that the groups differ by at least ε is rejected if the limits of the interval fall outside the $\pm\ \varepsilon$ bounds. Conversely, comparability is demonstrated when the bounds of the 90% confidence interval of the mean difference fall entirely within the $\pm\ \varepsilon$ bounds [42], [44].

Experiment	grippers without payload		grippers with payload	
	Average speed	Error	Average speed	Error
Point to point	804±107 μm/s	129±56 μm	1104±60 μm/s	236±44 μm
Circular	629±132 μm/s	123±95 μm	1081 ±42 μm/s	171±120 μm
Square	731±115 μm/s	93±104 μm	1089±49 μm/s	130±126 μm

TABLE I: Experimental motion control results of the grippers for point-to-point, circular and square trajectories. The average speeds and Euclidean-norm of average positioning error are reported with the respective standard deviation (150 and 15 experimental trials are conducted for grippers without and with the payload, respectively).

The design of equivalence tests can be tricky because the acceptance criterion ε must be defined on the basis of prior knowledge of the measurement. For a sample data set of p independent measurements with standard deviation δ, for instance, ε must certainly be greater than $\delta/\sqrt{p}$, otherwise the test may fail simply because of imprecision, rather than because of a true difference. However, it must also be less than any specifications or standards that the testing is challenging, or the test becomes too easy and will not adequately discriminate. In this work we evaluated ε as suggested in [42], where the authors provided a useful step-by-step process for performing equivalence testing with commonly available computational software packages. The two one-sided tests were performed between the eight grippers considered, and each circle and square they completed was considered as an independent observation, i.e., we tested 20 (trajectories) $\times$ 10 (grippers) = 200 error values. To avoid raising the family-wise error rate, i.e., the probability of at least one incorrectly rejected null hypothesis in a family of tests, we took into account the simple correction discussed in [45] and used in [43], [46]. The tests revealed statistical equivalence between 8 grippers. This suggests that the grippers behave similarly and their error in following a commanded trajectory is statistically negligible. Since 8 out of 10 grippers behaved similar we decided to use only loaded gripper for our motion experiments. This gripper executed five trials of the circular and square trajectory experiment and was used for five point-to-point motion control experiments. The gripper with the payload moved 52% faster than the grippers without the payload, with an average velocity and positioning error of 1091±73 μm/s and 171±236 μm, respectively. We attribute this increase in speed to the compact folded ball-shape of the gripper which reduces the shear forces with the water and the side-walls of the dish. The results of the loaded gripper are also tabulated in Table I and average motion for the square and circle trajectory can be seen in Fig. 18.

C. Pick-and-place experiment

In this experiment we evaluated the ability of the to pick-and-place micro-sized payloads. The grippers were positioned above a 500 μm micro-bead and then closed by regulating the water temperature to 40° C. This caused the gripper grasp the micro-bead. After capturing the micro-bead it was dragged to the desired drop off location to be released. The releasing procedure was activated by decreasing the temperature below 25° C. The pick-and-place experiment was repeated with 5 different grippers. A positioning error of 571±336 μm was achieved with an average execution time of 1811±239 s. The payload is transported for 1.5 cm with an average velocity of 1091±73 μm/s. Fig. 19 shows an example of a representative pick and place experiment.

D. Pick-and-place of biological tissue in a dynamic and cluttered environment

Based on a total of 5 trial this experiment was completed with an average execution time and drop off error of 130±39 s and 626±226 μm. These results were achieved with and average velocity of 1807±710 μm/s for loaded grippers and 2077±395 μm/s for unloaded grippers. Of the average execution time 25±9 s was used for grasping and 56±22 s for releasing of the egg yolk. The rest of the time was used for approach and transportation of the egg yolk. In non if the experiments the egg yolk was damaged from which we can conclude that the grippers are suited for a biopsy application. The high LDL content of the egg yolk and the fact that we performed the experiment on animal tissue in a dynamically cluttered environment shows that the grippers are promising for plaque removal from the arteries. Snapshots of a representative experiment can be seen in Fig. 20.

E. Autonomous micro-bead sorting experiment

During this experiment the tracking algorithm succeeded to demonstrate its capability to track micro-beads and precisely sort them based on color. A total of 5 trials of this experiment were conducted with an average execution time, velocity and drop off error of 437 ± 105 s, 1215 ± 681 μm/s and 850 ± 414 μm respectively. The average drop off error is within the bounds of the radius of the drop off location (1500 μm). Of the average execution time 99±37 s was used for grasping and 174±69 s for releasing of the micro-beads. The results

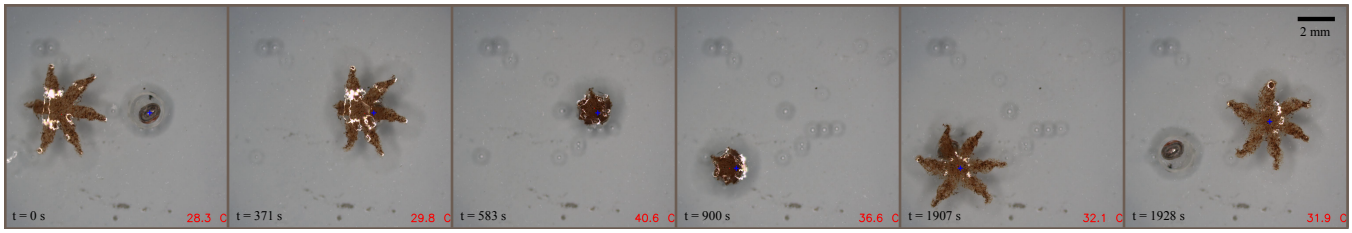

Fig. 19: Image sequence of a representative manual pick-and-place experiment. It can be seen that the gripper first approaches the micro-bead to arrive in opened configuration. When the gripper arrives at the microbead location the water temperature is regulated to approximately 40° C so that the gripper closes and grabs the microbead. Once the micro-bead is grabbed the setpoint of the gripper is changed to the desired drop off location. The micro-bead gets released at this location by cooling down the water do below 25° C. A total of five of these experiments were executed with an average execution time of 1811±239 s and an average drop off error of 573±336μ. The payload is transported for 1.5 cm with an average velocity of 1091±73 μm/s.The water temperature is indicated in red at the bottom right position of each image and the time of the snapshot is provided at the bottom left of each image. Furthermore in every image the blue cross shows the desired position of the gripper.

of this and the previous experiments have shown the ability of grippers to detect and adapt their behavior according to the surrounding environment. Fig. 21 shows snapshots of a representative autonomous micro-bead sorting experiment.

F. Haptic experiments

1) Experiment 1: From the first haptic experiment the following metrics are computed:

- Task completion time.
- Error in following the target trajectory with the reference point.
- Error in following the target trajectory with the gripper.
- Distance between the reference point and the gripper.
- Perceived effectiveness of each feedback condition.

In order to compare the different metrics, we ran a two-way repeated-measures ANOVA [47] on the data shown in Fig. 22. Presence of the inertia feedback (I) and type of feedback condition (Vs, Vs + Vb, Vs + Pc, and K) were treated as within-subject factors.

Figure 22a shows the average completion time for the eight experimental conditions. All the data passed the Shapiro-Wilk normality test [48] and the Mauchly's Test of Sphericity [49]. Sphericity was assumed for variables with only two levels of repeated measures. The two-way repeated-measure ANOVA revealed a statistically significant change in the completion time for inertia ($F(1,15) = 19.223, p = 0.001$, partial $\eta^2 = 0.562$) and feedback condition ($F(3,45) = 9.438, p < 0.001$, partial $\eta^2 = 0.386$). Post hoc analysis with Bonferroni adjustments [50] revealed a significant increase in the completion time for conditions providing visual and vibrotactile feedback on the error in following the target trajectory (Vs + Vb vs. Vs, $p = 0.013$; Vs + Vb vs. Vs + Pc, $p = 0.003$; Vs + Vb vs. K, $p = 0.002$). The Bonferroni correction is used to reduce the chances of obtaining false-positive results when multiple pair-wise tests are performed on a single set of data.

Figure 22b shows the average error in following the target trajectory with the reference point for the eight experimental conditions. It is calculated as the mean over time of $e_{rp} = \|\mathbf{p_r}(\mathbf{t}) - \mathbf{p_{t,r}}\|$, where $\mathbf{p_r}(\mathbf{t})$ is the position of the reference point as controlled by the user through the haptic interface, and $\mathbf{p_{t,r}}$ is the point on the target trajectory closest to $\mathbf{p_r}(\mathbf{t})$. All the data passed the Shapiro-Wilk normality test. Mauchly's Test of Sphericity indicated that the assumption of sphericity was violated for the feedback condition variable ($\chi^2(5) = 34.744, p < 0.001$). A Greenhouse-Geisser correction was applied to tests involving data that violate the sphericity assumption [51]. The two-way repeated-measure ANOVA revealed a statistically significant change in this error for inertia ($F(1,15) = 61.705, p < 0.001$, partial $\eta^2 = 0.804$) and feedback condition ($F(2,30.007) = 171.473, p < 0.001$, partial $\eta^2 = 0.920$). Post hoc analysis with Bonferroni adjustments revealed a significant difference in the error between all conditions (Vs vs. Vs + Vb, $p < 0.001$; Vs vs. Vs + Pc, $p < 0.001$; Vs vs. K, $p < 0.001$; Vs + Vb vs. Pc, $p < 0.001$; Vs + Vb vs. K, $p < 0.001$; Vs + Pc vs. K, $p < 0.001$).

Fig. 22c shows the average error in following the target trajectory with the gripper for the eight experimental conditions. It is calculated as the mean over time of $e_m = \|\mathbf{p_m}(\mathbf{t}) - \mathbf{p_{t,m}}\|$, where $\mathbf{p_m}(\mathbf{t})$ is the position of the gripper as evaluated by the tracking algorithm, and $\mathbf{p_{t,m}}$ is the point on the target trajectory closest to $\mathbf{p_m}(\mathbf{t})$. All the data passed the Shapiro-Wilk normality test. Mauchly's Test of Sphericity indicated that the assumption of sphericity was violated for the feedback condition variable ($\chi^2(5) = 34.744, p = 0.039$). A Greenhouse-Geisser correction was applied to tests involving data that violate the sphericity assumption. The two-way repeated-measure

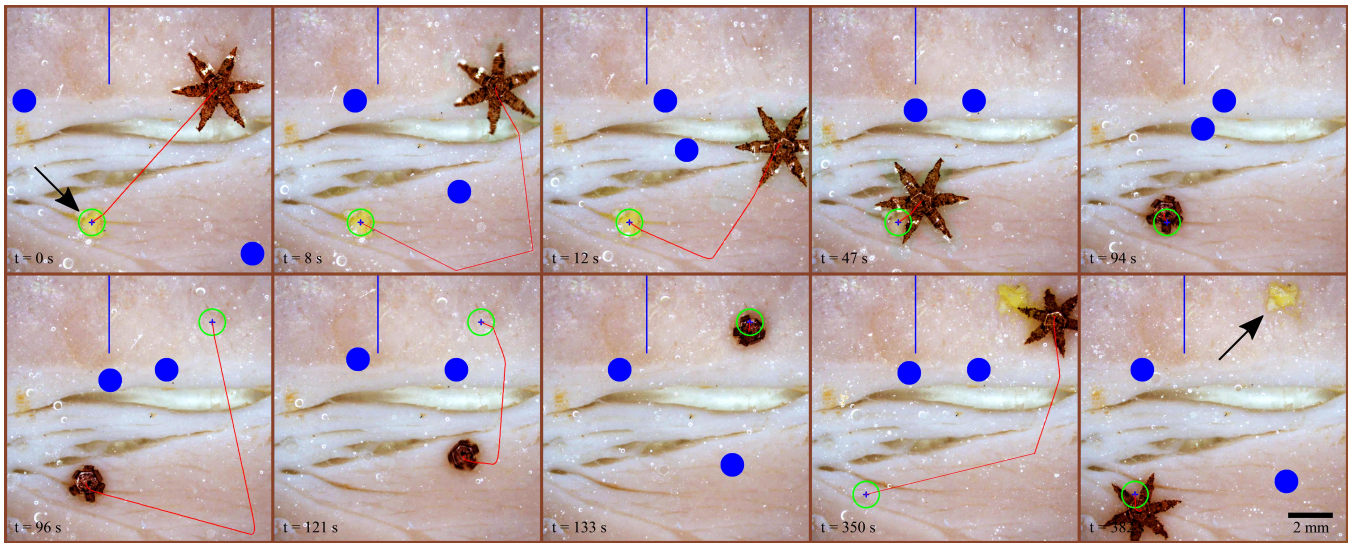

Fig. 20: Snapshots of a representative path planning experiment. During this experiment the gripper picked-and-placed a piece of biological material while avoiding one static and two dynamic virtual obstacles. The static obstacle is a wall of size 10×3500 μm. The dynamic obstacles are circles with radius 500 μm and velocity 300 μm/s and 425 μm/s. The red line shows the computed path by the path planner. In the first and last image the piece of biological material is pointed out by a black arrow. The time instance of the taken snapshot t can be seen at the bottom left corner of each image. The green circle in every image shows the setpoint of the gripper. Images 1-4 show that the path to the biological material is planned and that the gripper is steered towards it. From images 5-8 it can be seen that the biological tissue is grabbed and that the gripper is steered back to its starting position. From image 9 and 10 it can be seen that the biological material is dropped of successfully and the gripper is steered away. The average execution time and drop off error of 5 of these experiments are 130±39 s and 626±226 μm respectively. The experiments were executed with an average velocity of 1807±710 μm/s for loaded grippers and 2077±395 μm/s for unloaded grippers.

ANOVA revealed a statistically significant change in this error for inertia ($F(1,15) = 163.579, p < 0.001$, partial $\eta^2 = 0.916$) and feedback condition ($F(2.065, 30.9827) = 347.793, p < 0.001$, partial $\eta^2 = 0.959$). Post hoc analysis with Bonferroni adjustments revealed a significant difference in the error between all conditions (Vs vs. Vs + Vb, $p < 0.001$; Vs vs Vs + Pc, $p < 0.001$; Vs vs. K, $p < 0.001$; Vs + Vb vs. Vs + Pc, $p < 0.001$; Vs + Vb vs. K, $p < 0.001$; Vs + Pc vs. K, $p < 0.001$).

Fig. 22d shows the average distance between the reference point and the gripper for the eight experimental conditions. It is calculated as the mean over time of $d_{rf,m} = \|\mathbf{p_r(t)} - \mathbf{p_{m(t)}}\|$. All the data passed the Shapiro-Wilk normality test and Mauchly's Test of Sphericity. The two-way repeated-measure ANOVA revealed a statistically significant change in the distance for inertia only ($F(1,15) = 827.144, p < 0.001$, partial $\eta^2 = 0.982$).

After this analysis, we also tested whether the distance between the reference point and the gripper has any relationship with the measured error in following the target trajectory. Our hypothesis is that it is more effective to control the motion of the gripper when the reference point is close to it, leading to smaller errors. A Pearson's product-moment correlation was run to assess the relationship between this distance and the error in following the target trajectory with both the reference point and the gripper. Preliminary analyses showed the relationship to be linear with both variables normally distributed, as assessed by Shapiro-Wilk test, and there were no outliers. There was a strong positive correlation between the distance of the reference point and the gripper and both trajectory errors ($e_{rp} : r(14) = 0.797, p < 0.001$; $e_m : r(14) = 0.819, p < 0.001$).

In addition to the quantitative evaluation reported above, we also measured users' experience. Immediately after the experiment, subjects were asked to report the effectiveness of each feedback condition in completing the given task using a slider that ranged from 0 to 10, where a score of 0 meant "very low" and a score of 10 meant "very high". Fig. 22e shows the perceived effectiveness for the eight experimental conditions. All the data passed the Shapiro-Wilk normality test and Mauchly's Test of Sphericity. The two-way repeated-measure ANOVA revealed a statistically significant change in this error for inertia ($F(1,15) = 14.695, p = 0.002$, partial $\eta^2 = 0.495$) and feedback condition ($F(3,45) = 61.712, p < 0.001$, partial $\eta^2 = 0.804$). Post hoc analysis with Bonferroni adjustments revealed a significant difference in the error between feedback conditions Vs vs. Vs + Vb, $p < 0.001$; Vs vs. K, $p < 0.001$; Vs + Vb vs. Vs + Pc, $p < 0.001$; Vs

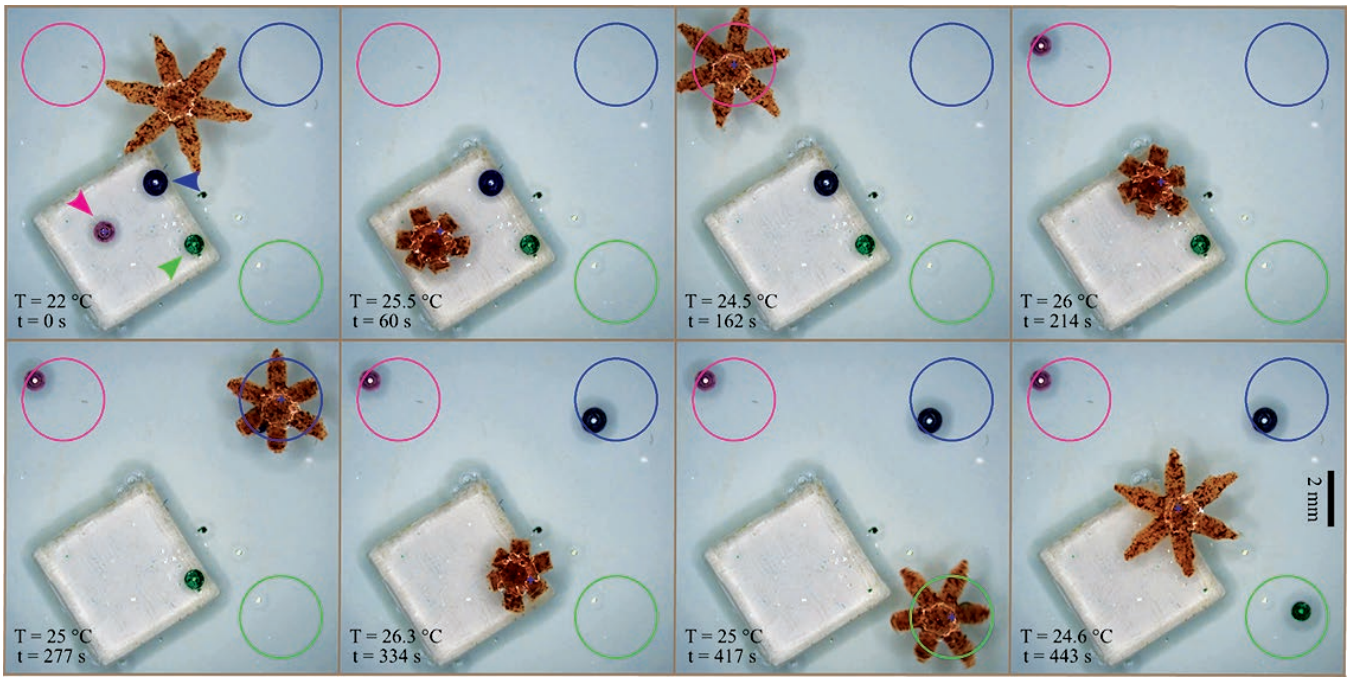

Fig. 21: Snapshots of a representative autonomous pick-and-place experiment. During this experiment the gripper autonomously sorted 3 different colored micro-beads with a radius of approximately 500 μm. In the first image the pink, blue and green micro-bead are pointed out by arrows of their respective colors. The colored circles in each image have a radius of 1500 μm and show the drop off locations of the three micro-beads. Water temperature T and the time instance of the taken snapshot t can be seen at the bottom left corner of each image. From the first 3 images it can be seen that the gripper first approaches the pink bead and subsequently drops it off at the desired drop off location. In images 4 to 8 it can be seen that this process is repeated for the blue and green micro-bead after which the gripper returns to a neutral position. The total operation time of this experiment was 443 seconds. The average time, velocity and drop off error of 5 of these experiments are 437 $\pm$ 105 s, 1215 $\pm$ 681 μm/s and 850 $\pm$ 414 μm respectively.

+ Vb vs. K, $p < 0.001$; and Vs + Pc vs. K, $p < 0.001$.

Finally, subjects were asked to choose the condition they preferred the most. Condition K+I was preferred by fourteen subjects and condition Vs was preferred by two subjects.

As an example Fig. 23 shows the position of the reference point (blue) and of the tracked gripper (red) along the x and y axes for target trajectory 1 (see Sec. IV-F.6). Average trajectory along the x and y axes (solid lines) $\pm$ standard deviation (patches) along the y axis is shown for each feedback condition. The target trajectory is plotted in black.

2) Experiment 2: From the second haptic experiment the following metrics are computed:

- Task completion time.
- Length path for the reference point.
- Length path for the gripper.
- Distance between the reference point and the gripper.
- Error in placing the micro-bead at the requested drop-off location.
- Perceived effectiveness of each feedback condition.

In order to compare the different metrics, we ran a one-way repeated-measures ANOVA on the data shown in Fig. 24. Type of feedback condition (K+I, V+I, and N) was treated as within-subject factors.

Fig. 24a shows the average completion time for the three experimental conditions. All the data passed the Shapiro-Wilk normality test and the Mauchly's Test of Sphericity. The one-way repeated-measure ANOVA did not reveal any statistically significant difference between the means.

Fig. 24b shows the average length of the path of the reference point for the three experimental conditions. All the data passed the Shapiro-Wilk normality test and Mauchly's Test of Sphericity. The one-way repeated-measure ANOVA revealed a statistically significant difference between the means ($F(2, 18) = 22.675, p < 0.001$, partial $\eta^2 = 0.716$). Post hoc analysis with Bonferroni adjustments revealed a significant difference in conditions K+I vs. N ($p = 0.001$) and V+I vs. N. ($p = 0.001$).

Fig. 24c shows the average length of the path of the gripper for the three experimental conditions. All the data passed the Shapiro-Wilk normality test and Mauchly's Test of Sphericity. The one-way repeated-measure ANOVA revealed a statistically significant difference between the means ($F(2, 18) = 20.518, p < 0.001$,

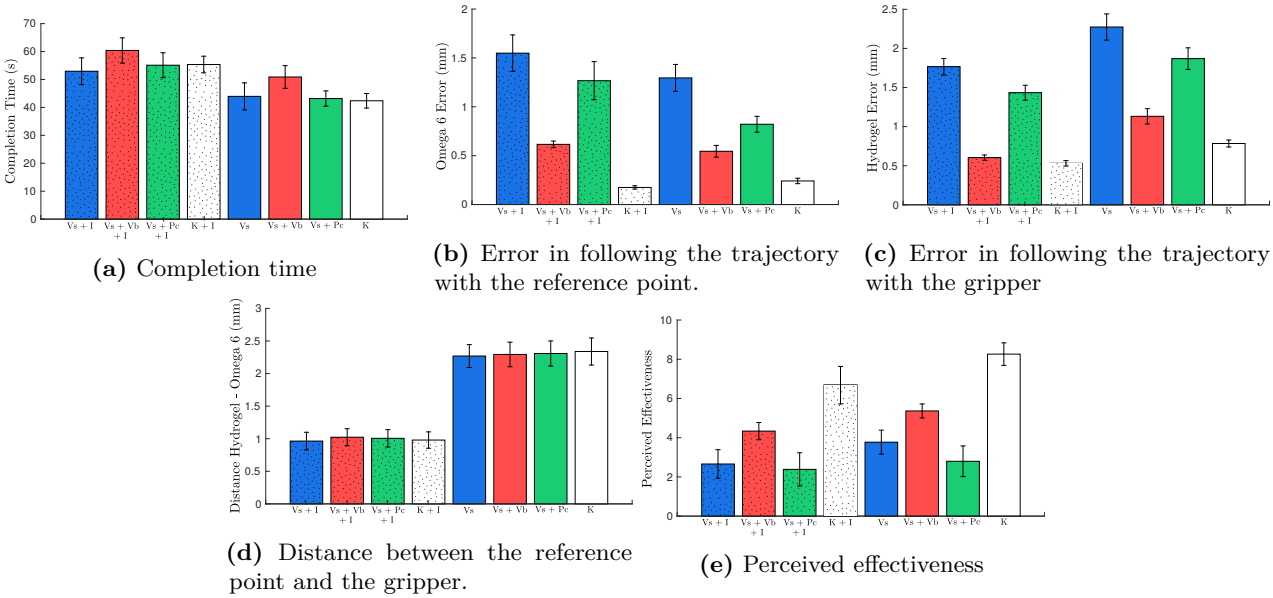

(a) Completion time

(b) Error in following the trajectory with the reference point.

(c) Error in following the trajectory with the gripper

(d) Distance between the reference point and the gripper.

(e) Perceived effectiveness

Fig. 22: Path following experiment: Completion time, error in following the trajectory with both the reference point and the gripper, distance between the reference point and the gripper, and perceived effectiveness for the eight considered feedback conditions are plotted (mean and 95% confidence interval).

partial $\eta^2 = 0.695$). Post hoc analysis with Bonferroni adjustments revealed a significant difference in conditions K+I vs. N ($p = 0.002$) and V+I vs. N. ($p < 0.001$).

Fig. 24d shows the average distance between the reference point and the gripper for the three experimental conditions. All the data passed the Shapiro-Wilk normality test and Mauchly's Test of Sphericity. The one-way repeated-measure ANOVA revealed a statistically significant difference between the means ($F(2, 18) = 134.252, p < 0.001$, partial $\eta^2 = 0.937$). Post hoc analysis with Bonferroni adjustments revealed a significant difference in conditions K+I vs. N ($p < 0.001$) and V+I vs. N. ($p < 0.001$).

Fig. 24e shows the average error in placing the micro-bead at the requested drop-off location for the three experimental conditions. All the data passed the Shapiro-Wilk normality test and Mauchly's Test of Sphericity. The one-way repeated-measure ANOVA did not reveal any statistically significant difference between the means.

In addition to the quantitative evaluation reported above, we also measured users' experience. Immediately after the experiment, subjects were asked to report the effectiveness of each feedback condition in completing the given task using a slider that ranged from 0 to 10, where a score of 0 meant "very low" and a score of 10 meant "very high". Fig. 24f shows the perceived effectiveness for the three experimental conditions. All the data passed the Shapiro-Wilk normality test and Mauchly's Test of Sphericity. The one-way repeated-measure ANOVA revealed a statistically significant difference between the means ($F(2, 18) = 22.275, p < 0.001$, partial $\eta^2 = 0.712$). Post hoc analysis with Bonferroni adjustments revealed a significant difference between all conditions (K+I vs. V+I, $p = 0.011$; K+I vs. N, $p = 0.001$; V+I vs. N, $p = 0.022$).

Finally, subjects were asked to choose the condition they preferred the most. Condition K+I was preferred by six subjects, while condition V+I was preferred by four subjects.

VI. Discussion

In order to explore new micro-robotic opportunities we employed soft magnetic micro-robots with grabbing dexterity for several tasks. In order to show the variability of opportunities of these untethered grippers we started with characterization of the grippers and then performed motion control and pick-and-place experiments. Subsequently we used the grippers for pick-and-place of biological material with high LDL content and the sorting of colored micro-beads. These experiments were executed in order to show more complicated tasks, exploit the soft properties of the grippers and approach more practical purpose.

Finally, in order to move towards more clinically accepted scenarios we then evaluated the effects of different types of haptic feedback on control of the grippers.

We characterized the grippers thermally and magnetically in order to investigate their response to heat and magnetic fields. We were interested in thermal characterization because the grasping functionality of the grippers is actuated by heat. We added and removed heat from the water in the petri-dish to open and close the grippers

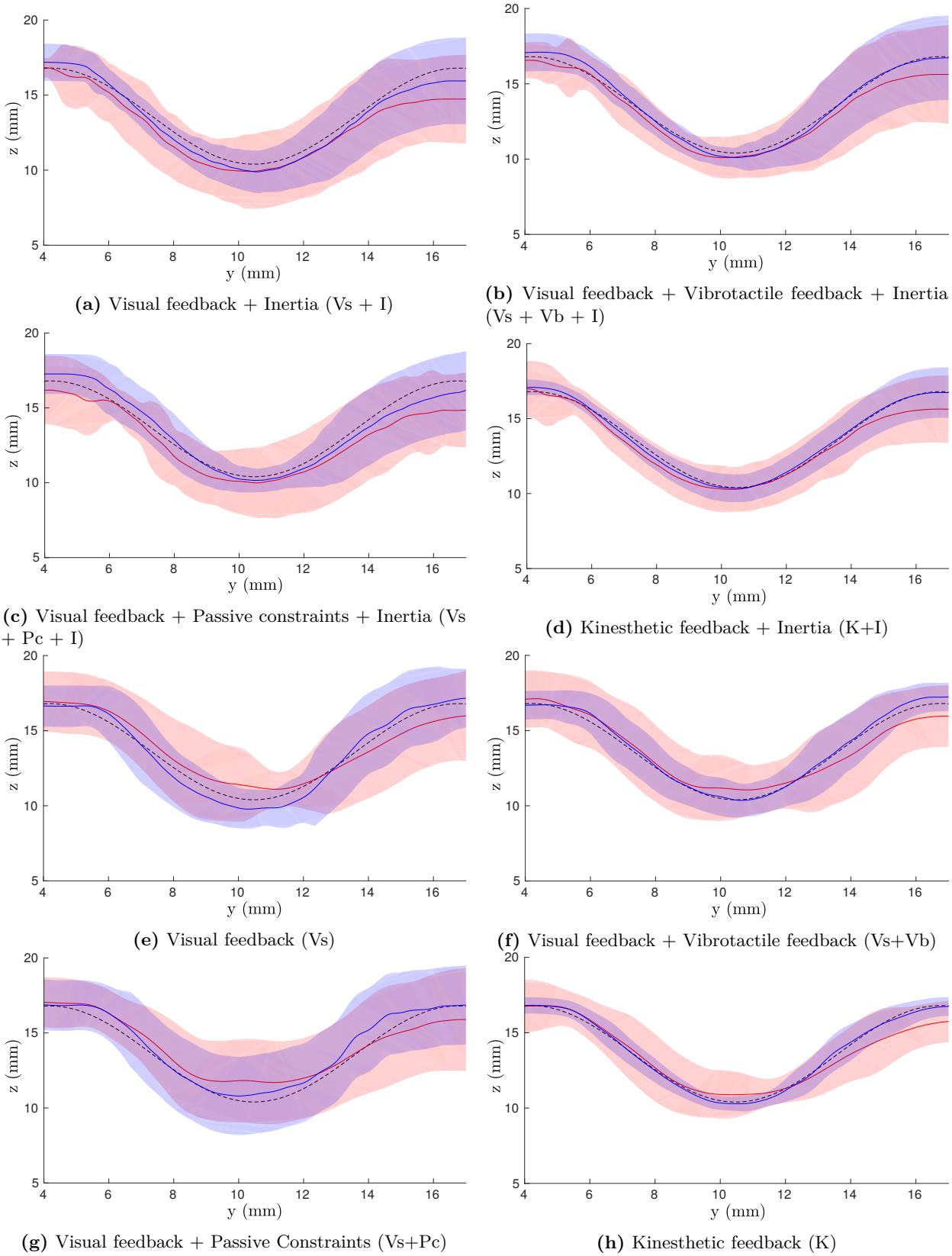

(a) Visual feedback + Inertia (Vs + I)

(b) Visual feedback + Vibrotactile feedback + Inertia (Vs + Vb + I)

(c) Visual feedback + Passive constraints + Inertia (Vs + Pc + I)

(d) Kinesthetic feedback + Inertia (K+I)

(e) Visual feedback (Vs)

(f) Visual feedback + Vibrotactile feedback (Vs+Vb)

(g) Visual feedback + Passive Constraints (Vs+Pc)

(h) Kinesthetic feedback (K)

Fig. 23: Path following experiment: Average trajectory of the reference point (blue) and the tracked gripper (red) along the x and y axes (solid lines) $\pm$ standard deviation (patches) along the y axis is shown for each feedback condition for the target trajectory (black dashed line).

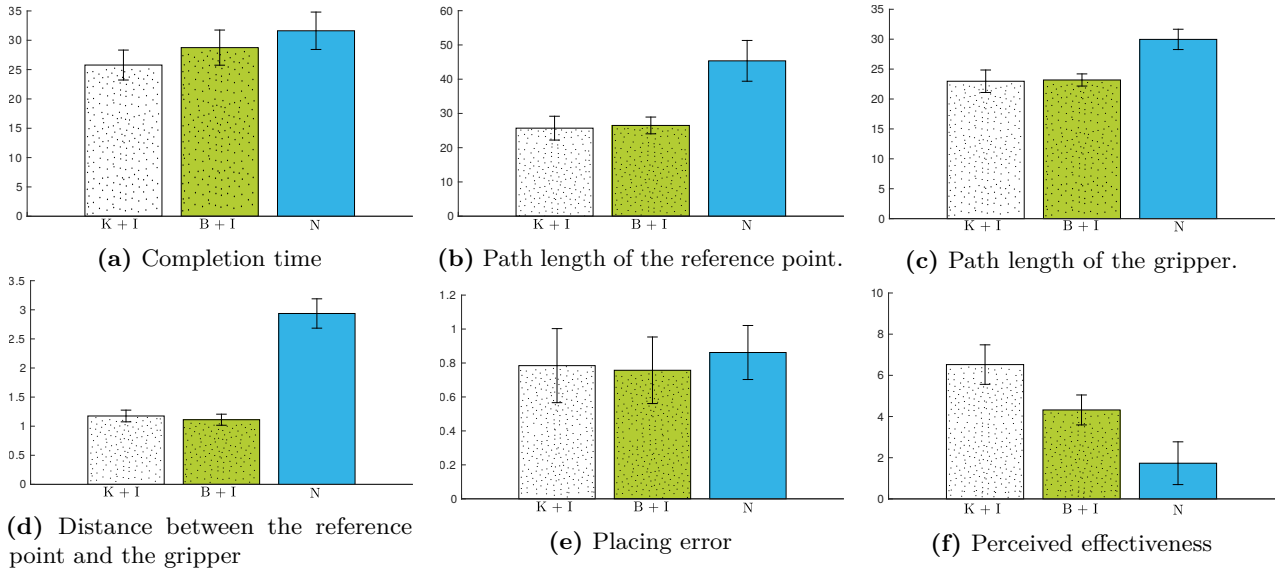

(a) Completion time

(b) Path length of the reference point.

(c) Path length of the gripper.

(d) Distance between the reference point and the gripper

(e) Placing error

(f) Perceived effectiveness

Fig. 24: Pick-and-place experiment. Completion time, path length for both the reference point and the gripper, distance between the reference point and the gripper, placing error, and perceived effectiveness for the three considered feedback conditions are plotted (mean and 95% confidence interval).

for five cycles. By using an image guided technique we then measured the microg-ripper configuration metric based on the length of its perimeter. The grippers on average completely opened at temperatures below 24 °C and fully closed above 27 °C. After more than 10 cycles the quality of the grippers decreased due to detachment of the SU8-layer. Once the SU8-layer starts to detach the grippers are unable to completely open.

Furthermore, before executing motion control experiments, we characterized the grippers magnetically by determining their magnetic dipole moment using U-turn experiments. Based on linear velocity and U-turn diameter we approximated the magnetic dipole moment of the grippers. For these experiments we assumed that the grippers had homogeneous iron-oxide patterning and that we could calculate the magnetic dipole moment of a six-tip dipole by superposing the magnetic dipole moment of 3 two-tip dipoles. We know that in practice the grippers not always have homogeneous iron-oxide patterning and that computing the magnetic dipole moment of a six-tip dipole is more complicated than superposition of 3 two-tip dipoles. However our resulting magnetic dipole moment was sufficient for accurate motion control of the grippers.

The motion control experiments consisted of point-to-point motion control and trajectory following for a circle and square trajectory for both loaded and unloaded grippers. During these experiments we were able to localize the grippers and have them follow trajectories with average positioning errors of 0.03 body lengths and speeds of 0.2 body lengths per second. We achieved the best results when the grippers were close to the water surface. This poses no problems for motion control but is disadvantageous for more complicated and practical experiments which require the folding functionality of the grippers. The gripper's tips have to deliver extra force to break through the water surface tension which requires addition of extra heat and slows down the grasping process. Also we noticed that the SU-8 layer of the grippers detached faster due to breaking through the water surface tension each time we executed a pick-and-place experiment.

During the pick-and-place experiments we transported 500 μm micro-bead for a distance of approximately 1.2 cm at average velocity of 1091$\pm$73 μm/s and positioning error of the payload of 571 μm. The experiment was carried out to show the added value of the grasping capabilities of our grippers. Due to the problem with overcoming the surface tension the grippers required extra heating to grasp the micro-bead. Also dragging the micro-bead across the bottom of the petri dish required strong magnetic field gradients. Patterning the grippers with a higher concentration of iron-oxide would enable the system to apply more magnetic force.

Since our grippers have soft properties they can be distinguished from previous micro-robots with grasping dexterity. We used the soft properties by employing the grippers for a pick-and-place task with egg yolk. We chose egg yolk due to its high LDL content which makes it comparable to the plaque which is removed from the arteries during endarterectomies. We were able to handle the egg yolk in a dynamic and cluttered environment. The grippers did not damage the very soft egg yolk which

showed that the grippers could also be used in a biopsy scenario. Due to lack of magnetic force we were not able to remove a piece of egg yolk from a larger lump of egg yolk. By using a permanent magnet however we were able do this which shows that stronger magnetic fields or higher concentration of iron-oxide patterning could realize this experiment within our set-up.

After showing ability to handle soft tissue we proved the ability of the system to recognize micro-beads of different color. With a decision making algorithm we were able to make the system autonomously sort the micro-beads. This experiment demonstrated a proof of concept for future recognition of light-colored plaque in the arteries but could also be seen as a first step for an automated micro-assembly application. Although we succeeded to carry out the experiment multiple times it was difficult execute it robustly. When the micro-beads where close together it was not possible to specifically pick the one of choice and also we used a small embankment (as can be seen in Fig. 21) to overcome issues relating to lack of sufficient magnetic force to drag the micro-beads along the bottom of the petri dish.

VII. Conclusions and future work

In this work we presented several applications for new biocompatible untethered soft micro-robots with grabbing dexterity. Using a high resolution camera and an image-guided tracking algorithm we were able to evaluate the position and configuration of these grippers at runtime. Six orthogonal electromagnets and a peltier element were used to control the position and configuration of the grippers. We experimentally evaluated our system (Fig. 1) by conducting experiments with precise motion control, pick-and-place tasks, handling of biological material and autonomous sorting of micro-beads.

A. Conclusions

This work showed advances in materials science and robotics which include

- The fabrication of reversible soft-actuating grippers that harness mechanical energy and shape change from swelling; hence they do not need wires, batteries or external power sources for actuation.
- The ability to control the local temperature and magnetic field in a closed-loop with high accuracy.
- Autonomous sorting on micro scale.

Applications for our grippers could be medical (e.g. biopsy or endarterectomies) or automated micro-assembly. The decision making and path planning algorithms in our obstacle avoidance and micro-bead sorting experiments investigated the potential of our grippers for a fully autonomous system that offers improved repeat-ability and response time in performing minimally invasive plaque removal operations. Keeping in mind the medical application, as a first step towards clinical employment of the grippers we also experimented with the effects of different types of haptic feedback on the control of the grippers. By keeping the surgeon in the control loop the grippers could be accepted more easily by patients.

B. Future work

In order to go into more realistic clinical scenarios in the near future experiments with smaller grippers should be carried out. For biopsy applications, since the sizes of cells are in the range of 10-100 microns, ideal sizes for the grippers would range from 10 μm to 1 mm [21]. Such sizes would also offer more maneuverability and access to smaller vessels. In addition, in order to be able to track and control the grippers in biological fluid, we plan on substituting the high-resolution camera with an ultrasound imaging system and investigate against the flow motion control. In this respect, [2] presented an algorithm for the closed-loop control of micro-motors using feedback extracted from B-mode ultrasound images, and [4] demonstrated the effectiveness of a wireless magnetic control system in steering the same micro-motors against fluidic flows. Finally 3-dimensional motion control will be investigated and we will move towards *in vivo* experiments.

VIII. Acknowledgments

I would like to thank my supervisors F. Ongaro, Dr. S. Scheggi, Dr. M. Abayazid and Prof. Dr. S. Misra for advising me during my work on this thesis. Also I would like to thank C. Yoon and Prof. Dr. D. H. Gracias from John Hopkins University for providing me with the soft grippers and Dr. C. Pacchierotti from Istituto Italiano di Tecnologia for the work with the haptic device.

References

[1] B. J. Nelson, I. K. Kaliakatsos, and J. J. Abbott, "Microrobots for minimally invasive medicine," *Annual review of biomedical engineering*, vol. 12, pp. 55–85, 2010.

[2] A. Sánchez, V. Magdanz, O. G. Schmidt, and S. Misra, "Magnetic control of self-propelled microjets under ultrasound image guidance," in *Biomedical Robotics and Biomechatronics (2014 5th IEEE RAS & EMBS International Conference on*, pp. 169–174, IEEE, 2014.

[3] I. S. Khalil, R. M. Metz, B. Reefman, S. Misra, *et al.*, "Magnetic-based minimum input motion control of paramagnetic microparticles in three-dimensional space," in *Intelligent Robots and Systems (IROS), 2013 IEEE/RSJ International Conference on*, pp. 2053–2058, IEEE, 2013.

[4] I. S. Khalil, V. Magdanz, S. Sanchez, O. G. Schmidt, and S. Misra, "The control of self-propelled microjets inside a microchannel with time-varying flow rates," *Robotics, IEEE Transactions on*, vol. 30, no. 1, pp. 49–58, 2014.

[5] I. S. Khalil, V. Magdanz, S. Sanchez, O. G. Schmidt, S. Misra, and E. Ben-Jacob, "Wireless magnetic-based closed-loop control of self-propelled microjets," *PloS one*, vol. 9, no. 2, p. e83053, 2014.

[6] I. S. Khalil, V. Magdanz, S. Sanchez, O. G. Schmidt, and S. Misra, "Three-dimensional closed-loop control of self-propelled microjets," *Applied physics letters*, vol. 103, no. 17, p. 172404, 2013.

[7] I. S. Khalil, V. Magdanz, S. Sanchez, O. G. Schmidt, and S. Misra, "Biocompatible, accurate, and fully autonomous: a sperm-driven micro-bio-robot," *Journal of Micro-Bio Robotics*, vol. 9, no. 3-4, pp. 79–86, 2014.

[8] I. Khalil, V. Magdanz, S. Sanchez, O. Schmidt, and S. Misra, "Biocompatible, accurate, and fully autonomous: a sperm-driven micro-bio-robot," *Journal of Micro-Bio Robotics*, vol. 9, no. 3-4, pp. 79–86, 2014.

[9] S. Martel, "Journey to the center of a tumor," *Spectrum, IEEE*, vol. 49, no. 10, pp. 48–53, 2012.

[10] K. E. Peyer, L. Zhang, and B. J. Nelson, "Bio-inspired magnetic swimming microrobots for biomedical applications," *Nanoscale*, vol. 5, no. 4, pp. 1259–1272, 2013.

[11] S. Sanchez, A. A. Solovev, S. Schulze, and O. G. Schmidt, "Controlled manipulation of multiple cells using catalytic microbots," *Chemical Communications*, vol. 47, no. 2, pp. 698–700, 2011.

[12] I. S. Khalil, F. van den Brink, O. S. Sukas, and S. Misra, "Microassembly using a cluster of paramagnetic microparticles," in *Robotics and Automation (ICRA), 2013 IEEE International Conference on*, pp. 5527–5532, IEEE, 2013.

[13] S. Martel and M. Mohammadi, "Using a swarm of self-propelled natural microrobots in the form of flagellated bacteria to perform complex micro-assembly tasks," in *Robotics and Automation (ICRA), 2010 IEEE International Conference on*, pp. 500–505, IEEE, 2010.

[14] S. R. Platt, J. Hawks, M. E. Rentschler, *et al.*, "Vision and task assistance using modular wireless in vivo surgical robots," *Biomedical Engineering, IEEE Transactions on*, vol. 56, no. 6, pp. 1700–1710, 2009.

[15] K. Harada, D. Oetomo, E. Susilo, A. Menciassi, D. Daney, J.-P. Merlet, and P. Dario, "A reconfigurable modular robotic endoluminal surgical system: vision and preliminary results," *Robotica*, vol. 28, no. 02, pp. 171–183, 2010.

[16] A. C. Lehman, N. A. Wood, S. Farritor, M. R. Goede, and D. Oleynikov, "Dexterous miniature robot for advanced minimally invasive surgery," *Surgical endoscopy*, vol. 25, no. 1, pp. 119–123, 2011.

[17] N. Bassik, B. T. Abebe, K. E. Laflin, and D. H. Gracias, "Photolithographically patterned smart hydrogel based bilayer actuators," *Polymer*, vol. 51, no. 26, pp. 6093–6098, 2010.

[18] C. Yoon, R. Xiao, J. Park, J. Cha, T. D. Nguyen, and D. H. Gracias, "Functional stimuli responsive hydrogel devices by self-folding," *Smart Materials and Structures*, vol. 23, no. 9, p. 094008, 2014.

[19] K. Malachowski, M. Jamal, Q. Jin, B. Polat, C. J. Morris, and D. H. Gracias, "Self-folding single cell grippers," *Nano letters*, vol. 14, no. 7, pp. 4164–4170, 2014.

[20] M. Jamal, A. M. Zarafshar, and D. H. Gracias, "Differentially photo-crosslinked polymers enable self-assembling microfluidics," *Nature communications*, vol. 2, p. 527, 2011.

[21] E. Gultepe, J. S. Randhawa, S. Kadam, S. Yamanaka, F. M. Selaru, E. J. Shin, A. N. Kalloo, and D. H. Gracias, "Biopsy with thermally-responsive untethered microtools," *Advanced Materials*, vol. 25, no. 4, pp. 514–519, 2013.

[22] S. Süsstrunk, R. Buckley, and S. Swen, "Standard rgb color spaces," in *Color and Imaging Conference*, vol. 1999, pp. 127–134, 1999.

[23] A. R. Smith, "Color gamut transform pairs," in *ACM Siggraph Computer Graphics*, vol. 12, pp. 12–19, 1978.

[24] M. W. Schwarz, W. B. Cowan, and J. C. Beatty, "An experimental comparison of rgb, yiq, lab, hsv, and opponent color models," *ACM Transactions on Graphics (TOG)*, vol. 6, no. 2, pp. 123–158, 1987.

[25] G. Reeb, "Sur les points singuliers dâĂŹune forme de pfaff completement intégrable ou dâĂŹune fonction numérique," *CR Acad. Sci. Paris*, vol. 222, pp. 847–849, 1946.

[26] C. L. Bajaj, V. Pascucci, and D. R. Schikore, "The contour spectrum," in *Proceedings of the 8th conference on Visualization'97*, pp. 167–ff, 1997.

[27] H. Carr, J. Snoeyink, and M. van de Panne, "Simplifying flexible isosurfaces using local geometric measures," in *Proc. Conference on Visualization*, pp. 497–504, 2004.

[28] S. Suzuki *et al.*, "Topological structural analysis of digitized binary images by border following," *Computer Vision, Graphics, and Image Processing*, vol. 30, no. 1, pp. 32–46, 1985.

[29] M. Y. Chan and F. Y. Chin, "General schedulers for the pinwheel problem based on double-integer reduction," *IEEE Transactions on Computers*, vol. 41, no. 6, pp. 755–768, 1992.

[30] F. Van Der Heijden, "Image based measurement systems: object recognition and parameter estimation," 1994.

[31] M. D. Heath, S. Sarkar, T. Sanocki, and K. W. Bowyer, "A robust visual method for assessing the relative performance of edge-detection algorithms," *IEEE Transactions on Pattern Analysis and Machine Intelligence*, vol. 19, no. 12, pp. 1338–1359, 1997.

[32] K. Bowyer and P. J. Phillips, *Empirical evaluation techniques in computer vision*. IEEE Computer Society Press, 1998.

[33] J. G. Ziegler and N. B. Nichols, "Optimum settings for automatic controllers," *trans. ASME*, vol. 64, no. 11, 1942.

[34] S. M. Lavalle, "Rapidly-exploring random trees: A new tool for path planning," tech. rep., Computer Science Dept., Iowa State University, 1998.

[35] S. M. LaValle and J. J. Kuffner, "Rapidly-exploring random trees: Progress and prospects," in *Algorithmic and Computational Robotics: New Directions*, pp. 293–308, 2000.

[36] F. Carpi and C. Pappone, "Magnetic maneuvering of endoscopic capsules by means of a robotic navigation system," *Biomedical Engineering, IEEE Transactions on*, vol. 56, no. 5, pp. 1482–1490, 2009.

[37] A. Bahaj, P. James, and F. Moeschler, "An alternative method for the estimation of the magnetic moment of non-spherical magnetotactic bacteria," *Magnetics, IEEE Transactions on*, vol. 32, no. 5, pp. 5133–5135, 1996.

[38] Y. Chemla, H. Grossman, T. Lee, J. Clarke, M. Adamkiewicz, and B. Buchanan, "A new study of bacterial motion: superconducting quantum interference device microscopy of magnetotactic bacteria," *Biophysical journal*, vol. 76, no. 6, pp. 3323–3330, 1999.

[39] R. W. Cholewiak and A. A. Collins, "Sensory and physiological bases of touch," *The psychology of touch*, pp. 23–60, 1991.

[40] M. Franken, S. Stramigioli, S. Misra, C. Secchi, and A. Macchelli, "Bilateral telemanipulation with time delays: a two-layer approach combining passivity and transparency," *IEEE Transactions on Robotics*, vol. 27, no. 4, pp. 741–756, 2011.

[41] C. B. Zilles and J. K. Salisbury, "A constraint-based god-object method for haptic display," in *Proceedings of the IEEE International Conference on Human Robot Interaction and Cooperative Robots*, vol. 3, pp. 146–151, 1995.

[42] G. B. Limentani, M. C. Ringo, F. Ye, M. L. Bergquist, and E. O. McSorley, "Beyond the t-test: statistical equivalence testing," *Analytical Chemistry*, vol. 77, no. 11, pp. 221–226, 2005.

[43] C. Pacchierotti, A. Tirmizi, and D. Prattichizzo, "Improving transparency in teleoperation by means of cutaneous tactile force feedback," *ACM Transactions on Applied Perception*, vol. 11, no. 1, pp. 4–4, 2014.

[44] C. Chen, N. Rathore, W. Ji, and A. Germansderfer, "Statisti-

cal equivalence testing for assessing bench-scale cleanability," *BioPharm International*, vol. 23, no. 2, 2010.

[45] C. Lauzon and B. Caffo, "Easy multiplicity control in equivalence testing using two one-sided tests," *The American Statistician*, vol. 63, no. 2, pp. 147–154, 2009.

[46] C. Pacchierotti, D. Prattichizzo, and K. J. Kuchenbecker, "Displaying sensed tactile cues with a fingertip haptic device," *IEEE Transactions on Haptics. In Press*, 2015.

[47] R. Gueorguieva and J. H. Krystal, "Move over anova: Progress in analyzing repeated-measures data andits reflection in papers published in the archives of general psychiatry," *Archives of general psychiatry*, vol. 61, no. 3, pp. 310–317, 2004.

[48] S. S. Shapiro and M. B. Wilk, "An analysis of variance test for normality (complete samples)," *Biometrika*, pp. 591–611, 1965.

[49] J. W. Mauchly, "Significance test for sphericity of a normal n-variate distribution," *The Annals of Mathematical Statistics*, vol. 11, no. 2, pp. 204–209, 1940.

[50] O. J. Dunn, "Multiple comparisons among means," *Journal of the American Statistical Association*, vol. 56, no. 293, pp. 52–64, 1961.

[51] S. W. Greenhouse and S. Geisser, "On methods in the analysis of profile data," *Psychometrika*, vol. 24, no. 2, pp. 95–112, 1959.